Hindawi
Advances in Meteorology
Volume 2022, Article ID 9070970, 29 pages
https://doi.org/10.1155/2022/9070970

Research Article

Comprehensive Evaluation and Error-Component Analysis of Four Satellite-Based Precipitation Estimates against Gauged Rainfall over Mainland China

Guanghua Wei,[1] Haishen Lü ,[2,3] Wade T. Crow,[4] Yonghua Zhu,[2,3] Jianbin Su,[5] and Li Ren[2,3]

[1]*School of Science, Jinling Institute of Technology, Nanjing 211169, China*
[2]*State Key Laboratory of Hydrology-Water Resources and Hydraulic Engineering, National Cooperative Innovation Center for Water Safety & Hydro-Science, College of Hydrology and Water Resources, Hohai University, Nanjing 210098, China*
[3]*Joint International Research Laboratory of Global Change and Water Cycle, Hohai University, Nanjing 210098, China*
[4]*USDA-ARS Hydrology and Remote Sensing Laboratory, Bldg. 007, Rm. 104, BARC-West, Beltsville, MD 20705-2350, USA*
[5]*Institute of Tibetan Plateau Research, Chinese Academy of Sciences, Beijing, China*

Correspondence should be addressed to Haishen Lü; haishenlu@foxmail.com

Received 5 September 2021; Revised 27 March 2022; Accepted 13 April 2022; Published 10 May 2022

Academic Editor: Federico Porcù

The Integrated Multi-Satellite Retrievals for Global Precipitation Measurement (IMERG) V06 product has been widely studied, but the errors and the source of the errors within IMERG over diverse climate regions still need to be quantified. To this end, the final run gauge-calibrated IMERG V06 (V06C) and uncalibrated IMERG V06 (V06UC) products are comprehensively evaluated here against 2088 precipitation gauges acquired between March 2014 and June 2018 over China. Moreover, V06C and V06UC rainfall estimates are compared against the Precipitation Estimation from Remotely Sensed Imagery using Artificial Neural Networks (PERSIANN)-Climate Data Record (CDR) and the Climate Prediction Center morphing technique (CMORPH) gauge-satellite blended (BLD) products. Continuous statistical indices and two error decomposition schemes are used to quantify their performance. Key results are as follows. (1) Except for V06UC's relatively high underestimation over the Tibetan Plateau (TP) and high overestimation over Xinjiang (XJ), Northeastern China (DB), and Northern China (HB) and CDR's severe overestimation over TP, all four satellite-based precipitation products can generally capture the spatial pattern of precipitation over China. Moreover, the satellite-based precipitation estimates agree better with gauge observations over humid regions than over semi-humid, semi-arid, and arid regions. (2) All the statistical indicators show that CDR has the worst performance, whereas BLD is the best precipitation product. As for the two IMERG products, V06C has improved V06UC's precipitation estimate. Results show that the gauge calibration algorithm (GCA) used in IMERG has active effect in terms of *r*, POD, and CSI. (3) Within all subregions, all four satellite-based precipitation products demonstrate their worst performance over the arid XJ region which exhibits the highest FAR and lowest POD and CSI values among all regions. (4) In terms of intensity distribution, for summer over China, the four satellite-based precipitation products generally overestimate the frequency of moderate precipitation and light precipitation events (<25 mm/day) and underestimate heavy precipitation events (>42 mm/day). (5) The relative bias ratio (RBR) analysis shows that the contribution of missed precipitation tends to be lower over wetter regions. In addition, for the same climate region, the contribution of missed precipitation is clearly lower in summer than in winter. In summer, false precipitation dominates the total error, whereas missed and false precipitation are the two leading error sources in winter. Future algorithm refinement efforts should focus on decreasing FAR in summer and winter and improving missed snow events during the winter.

1. Introduction

Droughts and floods are two particularly destructive natural disasters. Serious drought and flood hazards can cause heavy losses of lives and property damage [1–3]. For relevant emergency management of both drought monitoring and flood forecasting, reliable precipitation estimates are of vital importance [4].

Due to the uneven and sparse distribution of ground-based weather radars and rain-gauge networks, obtaining accurate spatiotemporal precipitation information has become a major challenge [5–10]. This issue is particularly relevant for China—especially for areas of Western and Northern China—with its complex topography and relatively uneven and sparse distribution of gauges and weather radars [8]. Fortunately, with the launch of new remote sensing satellites and the improvement of precipitation retrieval algorithms, new satellite-based precipitation products (SPPs) are constantly being developed and freely distributed. SPPs can offer near-real-time precipitation information and cost-effective information about the precipitation accumulation and distribution and the occurrence of area-average estimates over sub-catchments [11]. In addition, compared with conventional precipitation observation (gauges and weather radars), satellite-based precipitation estimates have more extensive spatial coverage and provide more continuous measurements [12–16].

To date, many satellite-based precipitation estimates, including the tropical Rainfall Measuring Mission (TRMM) Multi-Satellite Precipitation Analysis (TMPA) [17], the Precipitation Estimation from Remotely Sensed Imagery using Artificial Neural Networks (PERSIANN) [18], the National Oceanic and Atmospheric Administration (NOAA) Climate Prediction Center (CPC) morphing technique (CMORPH) [19], and the Integrated Multi-Satellite Retrievals for Global Precipitation Measurement (IMERG) [20–22], have been developed and released. In addition, researchers have recently made concerted efforts to evaluate and validate available remotely sensed precipitation products at the basin, regional, and global scale [7, 23–29]. Multiple researches have reported that SPPs have significant biases. Furthermore, due to the potentially nonlinear relationship between the precipitation and the hydrological process, such biases can be magnified in downstream hydrologic predictions when models are driven by satellite-based precipitation datasets [30–32]. Meanwhile, most prior researches have primarily focused on assessing the overall performance of satellite-based precipitation datasets. However, the exact source of precipitation retrieval error is also important for the evaluation of SPPs. Retrieving precipitation processes from satellite observations is composed of two separate steps: rain/no-rain recognition and precipitation rate estimation. Errors can arise in both steps.

If a given pixel cannot be correctly identified as rain or no rain, it will cause missed or false precipitation (termed as missed bias (−MB) and false bias (FB), respectively) respectively. When the raining pixels are correctly detected but precipitation rates are not precisely estimated in the second step, then the precipitation bias will be produced (termed as hit bias (HB)) [33]. Detailed descriptions of missed, false, and hit scenarios for the selected satellite-based precipitation against the gauged observations are introduced in Section 2.4.1. A missed scenario indicates that the precipitation signal is missed by satellite-based product but detected by gauged observation, a false scenario represents the opposite case of a missed scenario, and a hit scenario shows gauged observation and satellite-based product reporting precipitation events simultaneously. HB, −MB (missed precipitation (MP)), andFB (false precipitation (FP)) are always defined as satellite-based precipitation minus ground reference in respective scenario. Therefore, HB can be negative or positive. Likewise, −MB and FB are always negative and positive, respectively.

To track these various error contributions, Tian et al. [33] recommended an error-component analysis that decomposes the total bias (TB) of SPPs into three independent parts (hit bias, MP, and FP). According to the results of Tian et al. [33], the relation of the three independent error components (HB,−MB and FB) and total bias (TB) can be expressed as TB = HB − MB + FB. They [33] used such an analysis to evaluate six SPPs over the United States: TRMM 3B42 (TRMM Multi-Satellite Precipitation Analysis research product 3B42 Version 6), TRMM 3B42RT (TRMM Real-Time Multi-Satellite Precipitation Analysis experimental product), CMORPH, PERSIANN, NRL (Artificial Neural Networks Naval Research Laboratory's blended technique), and Higgins (NOAA/CPC near-real-time daily precipitation analysis). The study found that the three components were all substantial with great spatiotemporal variations. Tang et al. [34] also applied the analysis to investigate the TRMM errors over the United States and reported that hit bias had the largest contribution to the bias in the warm season and false and missed precipitation played an important role in the cold reason. In China, Yong [10] utilized error-component analysis to evaluate TRMM precipitation estimates. The results indicated that the error components in TMPA had remarkably seasonal and regional differences. Xu [35] used a decomposition assessment technique to trace the error sources of hourly IMERG during the warm season. The study pointed out that a large amplitude of false precipitation resulted in a serious overestimation for the precipitation of IMERG (more than 80%) over the eastern part of Mainland China. Both Ning et al. [36] and Su et al. [9] comprehensively evaluated the GSMAP (Global Satellite Mapping of Precipitation product) and IMERG over China by investigating the error features of GSMAP and compared them to two other SPPs. They found that GSMAP had a better performance than IMERG. Gebregiorgis et al. [37] found that the SPPs and hit bias were responsible for soil moisture error and runoff error, respectively. As revealed by the above studies, it is valuable to examine the error components of SPPs.

The IMERG product was updated to Version 06 in May 2019 [22]. Hereinafter, this new IMERG version is referred to as "IMERG V06." The IMERG V06 contains gauge-calibrated and uncalibrated products (termed as V06C and V06UC, respectively). Anjum et al. [38] compared IMERG V06 and V05 and TRMM 3B42 with gauge-based precipitation observations over the five hydro-climatologically distinct subregions in the Tianshan mountains. The result showed that IMERG V06 had no obvious improvements in comparison with IMERG V05. Jiang et al. [39] evaluated the utility of evapotranspiration products and IMERG V06 for drought monitoring over Mainland China. The study pointed out that the performances of the Standard Precipitation Evapotranspiration Index over Southwest China

and eastern China were significantly superior to their performances in the XB, TP, and XJ subregions. Wei et al. [40] assessed the suitability of IMERG V06 for drought monitoring over China and reported that the IMERG V06 has a good drought monitoring ability. Ma et al. [41] evaluated the accuracy of TRMM Version 7 and IMERG V06 at 677 stations over Mainland China. The research showed that IMERG had a better performance over semi-humid regions than over arid regions. Tang et al. [42] conducted a comprehensive comparison of IMERG V06 with nine satellite and reanalysis products over Mainland China. Their study showed that IMERG V06 had better performance than CDR. In addition, other studies have evaluated IMERG precipitation products from different perspectives and obtained many useful results [43–46]. However, the IMERG V06 product in particular has not been well evaluated by error decomposition technique over diverse climate regions in Mainland China. With its large land area, diverse climate, and complex topography (Wei et al. [8]), China is very suitable for the evaluation of the quality of new SPPs. Our goal is to obtain new insight into IMERG's comprehensive error features and offer useful evaluation information for both data users and IMERG algorithm developers.

2. Study Areas, Datasets, and Methodology

2.1. Study Areas. The study area focuses on areas of Mainland China located between 73° and 135°E and 18°–53°N (Figure 1). China is dominated by complex topography with highly variation and diverse climates. Xie et al. [47] and Shen et al. [48] pointed out that the satellite-based precipitation agreed well with gauge observations over humid regions of China but generally demonstrated poor performance over arid and semi-arid regions. Gebregiorgis et al. [37] also found that climate regime and topography played a key role in the performance of SPPs. In order to better compare SPPs, the whole of Mainland China is divided into eight subregions according to the principles (i.e., mountain ranges, the annual average precipitation distribution and elevation, etc.) suggested by Chen et al. [49].

These eight subregions are arid Xinjiang (XJ); cold Qinghai-Tibetan Plateau (TP); semi-arid Northwestern China (XB); semi-humid Northeastern China (DB) and Northern China (HB); and humid southwest Yungui Plateau (YG), Yangtze River (CJ) Plain, and Southeastern China (HN) regions. The key characteristics of these eight subregions are provided in Appendix A. For more detailed features and information in this regard, see Wei et al. [8] and related studies [12, 13, 15, 24, 25, 49].

2.2. Gauge Precipitation Observations. The RV06C, CDR, and BLD precipitation products were blended with different gauge precipitation observations (less than 400 China's international exchange stations over the country). Here, in order to avoid any misleading results, those gauge observations which had been adopted to calibrate the four SPPs were excluded from the reference data we applied for validation purpose. On this basis, the 2088 in situ gauges were selected. Furthermore, selected gauges contained no missing values during the study period from 12 March 2014 to 30 June 2018. Figure 1 shows the spatial distribution of the rain stations. All gauges make hourly measurements of rainfall accumulation. Based on these measurements, the China Meteorological Administration (CMA) provided and calibrated the daily precipitation datasets of 2088 separate automatic meteorological stations. The strict quality control of gauge data in three levels included extreme value masking, removal of questionable data, and internal consistency checks performed by the National Meteorological Information Center (NMIC) [30, 50]. Here, the daily precipitation of gauge observations was defined as accumulated precipitation depth every 24 hours from 0 : 00 to 23 : 59 UTC.

2.3. Satellite-Based Precipitation Datasets

2.3.1. BLD. The CMORPH products are based on the NOAA Climate Prediction Center's morphing technique. The existing microwave rainfall algorithms are used for CMORPH. In this process, the motion vectors obtained from half-hour interval geostationary satellite infrared imagery are used to propagate the relatively high-quality precipitation estimates obtained from passive microwave data.

CMORPH provides three types of rainfall products: (i) a satellite-only precipitation product (RAW), (ii) a bias-corrected product (CRT), and (iii) a gauge-satellite blended product (BLD). Here, based on the CPC unified daily gauge analysis and the RAW product, NOAA/CPC produced the CRT precipitation product by utilizing the probability density function matching to perform bias reduction over land. Then, a gauge analysis (about 300 to 400 China's international exchange stations over the country) based on an optimal interpolation technique is applied to the CRT product to generate the BLD product. The $0.25° \times 0.25°$/daily BLD global precipitation estimates from 60°N to 60°S were first released in 1998. For a full description of the CMORPH algorithm and its applications, see Joyce et al. [51] and Habib et al. [52]. Here, the BLD precipitation datasets were downloaded from ftps://ftp.cpc.ncep.noaa.gov/precip/ and examined between 12 March 2014 and 30 June 2018.

2.3.2. CDR. Based on the Climatic Data Center Climate Data Record program, NOAA designed the PERSIANN-Climate Data Record (termed as CDR) precipitation product [53]. The latest CDR version utilizes local cloud textural information from GridSat-B1 infrared (IR) data to train the PERSIANN model. In order to improve upon the accuracy of the product, the Global Precipitation Climatology Project (GPCP) monthly 0.25° product version 2.2 (less than 380 China's international exchange stations over the country) was adopted to remove monthly bias in PERSIANN precipitation estimates. The daily CDR product covers an area from 60°N to 60°S latitude at a spatial resolution of $0.25° \times 0.25°$. For this study, CDR precipitation datasets were downloaded from ftps://persiann.eng.uci.edu/pub/ and examined between 12 March 2014 and 30 June 2018. For

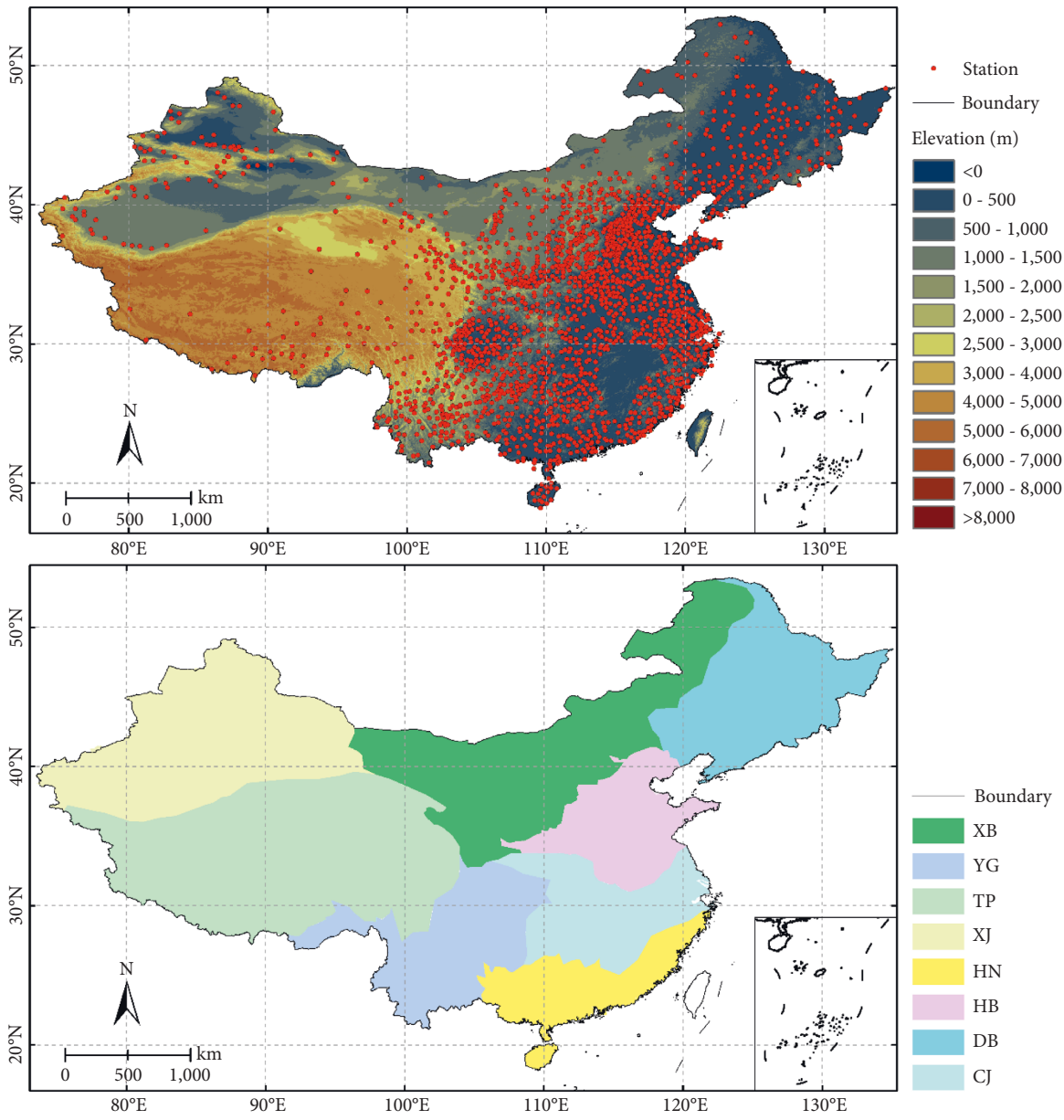

Figure 1: Map of our eight subregions of interest: the Xinjiang region (XJ), the Qinghai-Tibetan Plateau (TP), Northwest China (XB), the southwest Yungui Plateau (YG), Northeastern China (DB), Northern China (HB), the plain region of Yangtze River (CJ), and Southeastern China (HN) and the spatial distribution of ground-based rain gauges within China.

more detailed information regarding CDR, see Ashouri et al. [54].

2.3.3. IMERG. The American National Aeronautics and Space Administration (NASA) and the Japan Aerospace Exploration Agency (JAXA) opened the Global Precipitation Measurement (GPM) mission in 2014. Since the GPM Core Observatory satellite was launched on February 27, 2014, IMERG products have undergone a series of major revisions and reanalysis including the latest release of IMERG Version 6 in May 2019 [22]. IMERG V06 contains three types of precipitation products: (i) an early run precipitation product with a latency of 4 hours, (ii) a late run product with a latency of 12 hours, and (iii) a final run product with a latency of about 4 months. The IMERG V06 product at $0.1^{\circ} \times 0.1^{\circ}$ spatial and half-hour temporal resolution provides global precipitation estimates from 90°N to 90°S. For a more detailed introduction regarding CMORPH and IMERG, see Wei et al. [8]. For more detailed information regarding IMERG algorithm, see the IMERG Algorithm Theoretical Basis Document [21]. Here, IMERG V06 precipitation product datasets during the study period from 12 March 2014 to 30 June 2018 were obtained from https://pmm.nasa.gov/data-access/downloads/gpm.

The final run half-hourly IMERG V06UC and IMERG V06C products with a spatial resolution of $0.1^{\circ} \times 0.1^{\circ}$ between March 2014 and June 2018 were employed in this study. The

final run IMERG V06C product was calibrated via comparisons with the GPCC (Global Precipitation Climatology Center) precipitation dataset (only using data from 194 China's international exchange stations over the country). Daily IMERG precipitation estimates were produced by summing all 48 half-hourly precipitation accumulation products. The near real-time IMERG products, including early run and late run products, also need to be evaluated, given their widespread application in disaster forecasting and hydrometeorological modeling. Future researches investigating this aspect should be recommended.

2.4. Methodology

2.4.1. Statistical Analysis. The inverse distance weighting (IDW) interpolation method has been widely applied to obtain the spatial rainfall distribution in previous research [7, 55–57]. Here, for a fair comparison, the IDW interpolation method was utilized to resample both calibrated IMERG V06C and uncalibrated IMERG V06UC from a $0.1^\circ \times 0.1^\circ$ to a $0.25^\circ \times 0.25^\circ$ grid. Hereinafter, the resampled IMERG precipitation estimates are referred to as RV06C and RV06UC, respectively. For a more detailed description of the IDW interpolation method, see Wei et al. [7, 8].

Overall, BLD, CDR, RV06C, and RV06UC from 12 March 2014 to 30 June 2018 were employed in this paper. The four SPPs were comprehensively evaluated against the gauge precipitation estimates (2088 precipitation gauges) with the conventional statistical method and the error-component analysis technique over Mainland China. Prior to this comparison, all four SPPs were aggregated to a daily temporal and onto a uniform 0.25° spatial grid.

Many prior studies have utilized ground-based daily or monthly precipitation observations to assess the quality of SPPs [12–15]. Here, all four SPPs (BLD, CDR, RV06C, and RV06UC) were evaluated at grid-boxes during the period from March 2014 to June 2018. For the analysis, only the grids of SPPs containing the in situ gauging stations were chosen. In cases where the center of grid was close to the gauging station, a direct comparison was conducted between the SPPs and the corresponding gauge observation precipitation. In cases where the gauging station was surrounded by four grid cells but not particularly near to the center of any, an average of the four satellite grid precipitation estimates was utilized for comparison with the corresponding gauge observation. The daily precipitation classes followed China Meteorological Administration as follows: (1) rain < 10 mm/day (light rain); (2) 10 mm/day-$\leq$ rain < 25 mm/day (moderate rain); (3) 25 mm/day-$\leq$ rain < 50 mm/day (heavy rain); (4) rain ≥ 50 mm/day (violent rain).

The four traditional statistical indices Pearson linear correlation coefficient (r), relative bias (RB), mean absolute error (MAE), and root mean square error (RMSE) were used to quantitatively assess the overall performance of the four SPPs. Meanwhile, a contingency table that monitors the frequency of rain/no-rain estimates in both gauge and satellite-based precipitation was also employed (see Appendix B). A complete description of these statistical metrics can be found in Wei et al. [7, 8], Chen and Li [15], and Tan et al. [58]. Here, a threshold of 1 mm/day was adopted to determine the occurrence of precipitation for any given day when computing categorical metrics.

The equations for continuous and categorical verification metrics are listed in Appendix C—where G_i andS_i represent the values of the rain-gauge measurement and satellite grid precipitation estimate for the ith day, respectively; $\overline{G}$ and$\overline{S}$ are the average values of the reference precipitation and satellite precipitation, respectively; n is the total number of observations from the rain station or satellite-based precipitation estimate; M denotes the total number of days when observed precipitation is not detected by satellite product; H is the total number of days when observed precipitation is correctly detected by satellite-based precipitation product; and F reflects the total number of precipitation events that are detected by satellite product but not by the rain station. All metrics are computed only for grid-boxes in which rain stations are located.

A detailed description of the error decomposition and relative bias ratio is provided in Appendix D.

3. Results and Analysis

3.1. Spatiotemporal Analyses of Average Precipitation in China. To examine the accuracy with regard to capturing precipitation amounts from March 2014 to June 2018, the spatial distributions of average daily precipitation values obtained from the four SPPs and the rain-gauge observations are shown in Figure 2.

Generally speaking, all the four SPPs can capture the spatial patterns of average daily precipitation amounts over Mainland China against gauge observations. Meanwhile, all products in Figure 2 accurately reflect the general increasing trend of precipitation from the northwest and northeast to the southeast coast, illustrating that the characteristics of precipitation vary with elevation, longitude, latitude, diverse climate, complex terrains, etc.

However, finer-scale differences can be observed between the satellite-based products. For instance, the V06UC precipitate estimate shows less precipitation than the other three SPPs along the southwest border in the YG mountainous subregion. In addition, RV06UC estimates less precipitation than other SPPs in areas bordering CJ and HN and east of DB. However, CDR tends to have estimate more precipitation than the other four SPPs over the XJ subregion according to Figures 2(a)–2(e)—indicating that the current SPPs tend to have greater uncertainty in high-altitude areas, and there is still room for algorithm improvement in SPPs.

Impressively, BLD precipitation estimates show very high accumulated maxima at sporadic individual pixels. On the contrary, both the IMERG and CDR products have a smoother precipitation pattern. The former observation is perhaps due to the IMERG product's finer spatiotemporal resolution (0.1°/half hour) [15] and the additional microwave signals used in the IMERG products which objectively improve the precipitation retrieval accuracy. The latter

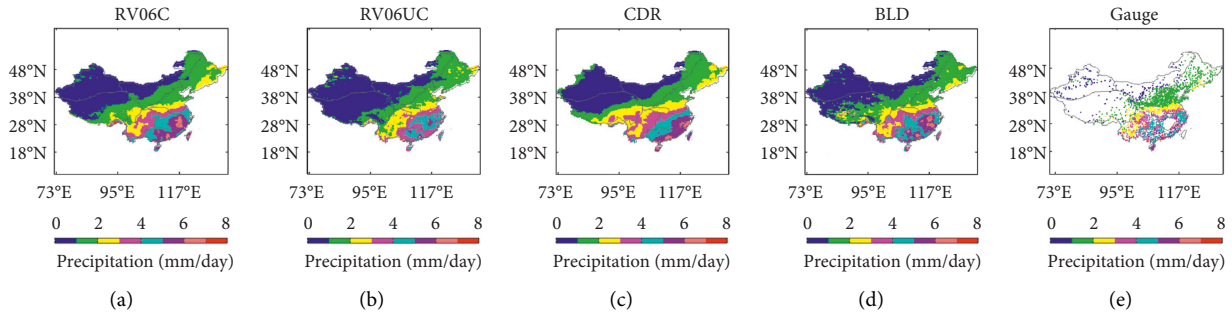

Figure 2: Spatial distribution of average daily precipitation (mm/day) derived from (a) RV06C, (b) RV06UC, (c) CDR, (d) BLD, and (e) in situ gauges over Mainland China from March 2014 to June 2018.

observation is attributed to the Artificial Neural Networks employed in CDR.

To further analyze the temporal characteristics of average daily precipitation over Mainland China, the time series of average daily precipitation obtained from the four SPPs and the corresponding gauge-based observations during the study period (from March 2014 to June 2018) are depicted in Figure 3. A 31-day running average is utilized to the mean daily precipitation time series to reduce visual clutter. Palomino-Angel et al. [59] and Anjum et al. [38] compared the reference and satellite-based mean daily precipitation by the same method.

In general, all four SPPs can reproduce the temporal characteristics of the gauge-based observations. The period (June to August) of maximum precipitation was identified. However, the estimated daily precipitation data (from SPPs) varied more than the observed precipitation data (from gauges). According to Figure 3 and the mean of the average daily precipitation time series (2.767 mm/day for RV06C, 2.735 mm/day for RV06UC, and 2.5772 mm/day for rain-gauge observations), RV06C and RV06UC precipitation estimates share a similar distribution in the year, and both IMERG products overestimate precipitation estimates acquired from gauge observations in rainy season (from June to August). However, CDR tends to show a larger overestimation from March to September according to Figure 3 and the mean average daily precipitation time series (2.7804 mm/day for CDR, 2.5772 mm/day for rain gauges). In the end, Figure 3 and the average rainfall closest to the station among the four SPPs (2.6643 mm/day for BLD and 2.5772 mm/day for gauge) indicate that BLD captures the rainfall of the rain-gauge observations best. However, it still suffers from some periodic biases.

To quantitatively compare average daily precipitation, r, RB, MAE, and RMSE metrics for RV06C, RV06UC, CDR, and BLD mean daily precipitation estimates throughout the entire study period (from March 2014 to June 2018) over Mainland China and the selected eight subregions are shown in Figure 4.

According to Figure 4(a), BLD has the highest r values among the four SPPs for all regions. Likewise, in comparison with the other satellite-based products, CDR shows the lowest r values in all regions. This result may be related to the fact that rain-gauge data is used to bias-correct BLD at the daily scale and CDR at the monthly scale. As for the r values of the calibrated RV06C and uncalibrated RV06UC products, RV06C looks better than RV06UC as the r values of V06C are higher than those of V06UC for all regions. Furthermore, among all regions, each satellite-based precipitation product shows the lowest r over the arid XJ region due to its complex topography and sparse rain-gauge coverage. With regard to RBs for the two IMERG products, the uncalibrated RV06UC exhibits higher positive RBs (32.76% over XJ, 17.46% over XB, 28.47% over DB, and 27.02% over HB) and larger negative RB (−25.66%) over TP. However, the calibrated RV06C product improves upon RV06UC's overestimation and underestimation with RBs falling to 4.66% over XJ, 10.48% over XB, 15.24% over DB, 11.52% over HB, and 11.15% over TP. It therefore appears that the gauge adjustment algorithm in RV06C has partially corrected systematic biases. However, the overestimation of rainfall remains in the RV06C product and cannot be ignored, especially over XJ, XB, DB, and HB, where the RBs are above 10%. However, the RB for RV06UC is smaller than RV06C, which may be related to negative RBs (over TP, YG, and HN) offsetting a portion of positive RBs (over XJ, XB, DB, HB, CJ) for RV06UC. Meanwhile, for RV06C, RBs are always positive. Among the four satellite-based products, RV06UC shows the highest absolute RBs over XJ, XB, YG, DB, HB, and CJ. Meanwhile, CDR has the highest RBs over Mainland China and HN, especially over TP with RB value of 50.8%. In the end, among the four SPPs, BLD shows the smallest RBs over most regions, such as China, TP, DB, HB, CJ, and HN.

With regard to MAE and RMSE, BLD has the lowest MAEs and RMSEs regardless of region and CDR shows the highest MAEs and RMSEs over Mainland China, TP, XB, YG, CJ, and HN among the four SPPs. The calibrated RV06C and uncalibrated RV06UC precipitation estimates exhibit similar performance. At the same time, V06C has slightly smaller MAEs and RMSEs than RV06UC over XJ, XB, DB, HB, and CJ and has a bit larger MAEs and RMSEs than RV06UC over other subregions. In general, RV06C shows slightly better performance than RV06UC with smaller MAE (0.9661 vs. 1.0101) and RMSE (1.424 vs. 1.4937) over Mainland China. In addition, the MAE and RMSE vary greatly over the eight subregions for the heterogeneity of precipitation accumulation. Generally speaking, MAE and

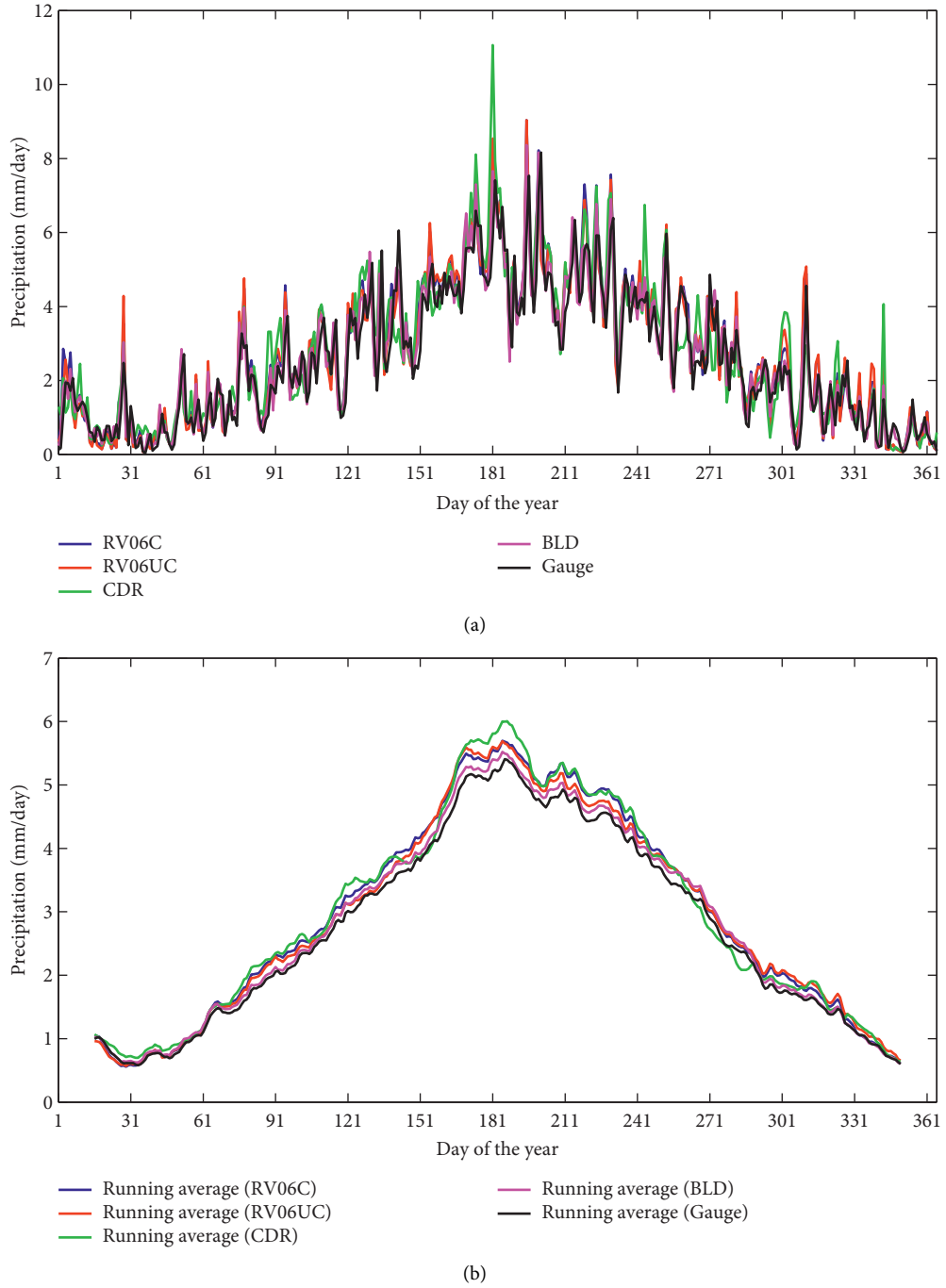

FIGURE 3: Comparison of average daily precipitation time series derived from the four SPPs and the corresponding gauge observations over Mainland China during the period from March 2014 to June 2018 (a). A 31-day moving average is utilized to each average daily precipitation time series to reduce visual cluttering (b).

RMSE values for the humid regions (YG, CJ, and HN) and semi-humid regions (DB and HB) are higher than those for the arid XJ, semi-arid XB, and cold TP regions.

In summary, among the four SPPs, it can be seen that CDR performs the worst with the lowest r values in all regions, the highest RMSEs (except for XJ, DB, and HB subregions) and MAEs (except for XJ and DB), and the largest RB within all of Mainland China. The CDR's poor performance has been noted previously by Tang [42]. As for the two IMERG products, RV06C has slightly improved RV06UC's precipitation estimates according to the relatively larger r values regardless of region and smaller RMSEs and MAEs over China and most subregions (HB, DB, XB, XJ, and CJ). As for BLD, it is the best of the four SPPs with the highest r values and the lowest MAEs and RMSEs over each region and RBs over most regions (China, HB, XB, DB, TP, HN, and CJ). These results are consistent with the results shown in Figure 3.

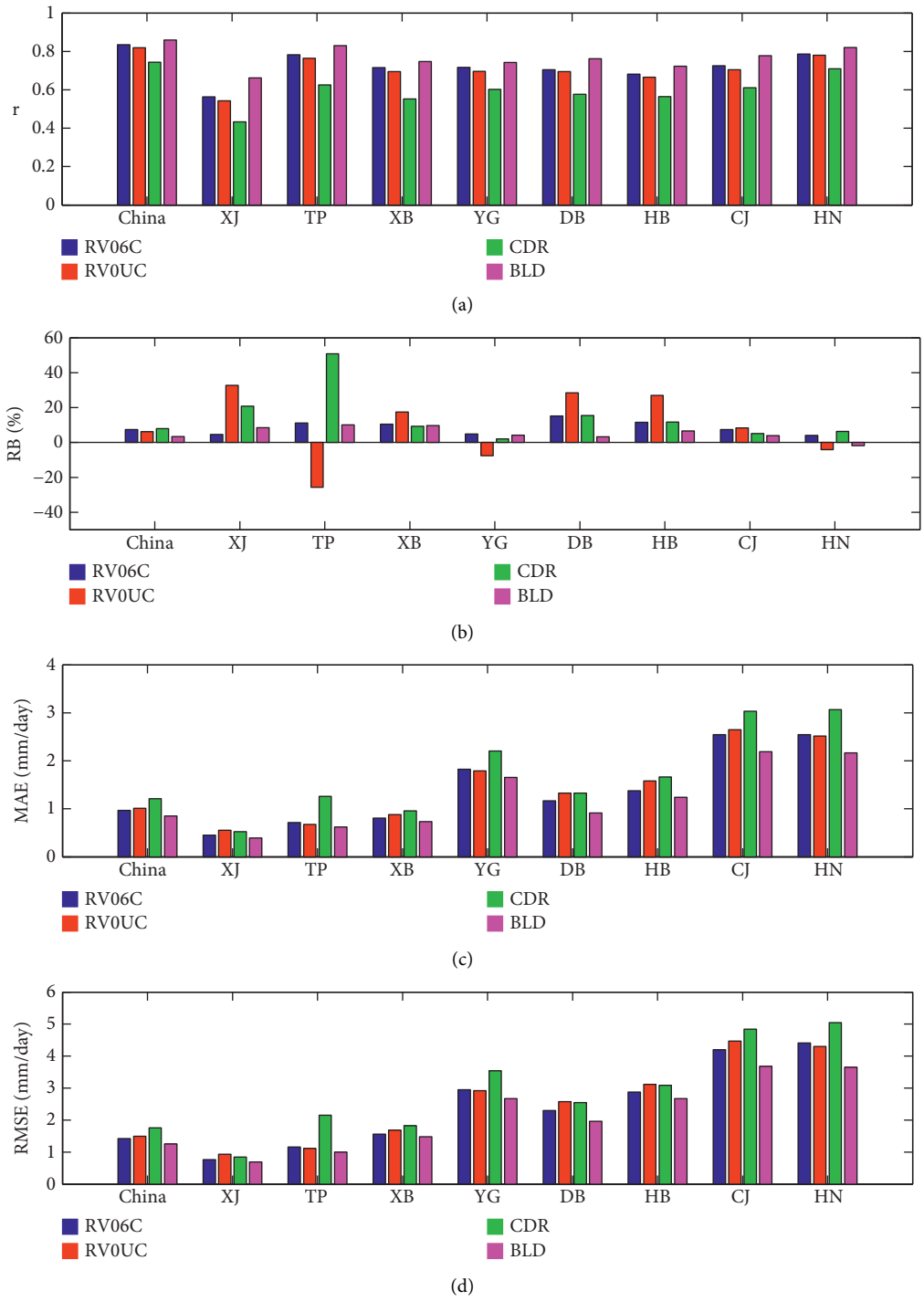

Figure 4: Values of *r*, RB, MAE, and RMSE performance metrics for mean areal precipitation estimate time series derived from RV06C, RV06UC, CDR, and BLD during the period from March 2014 to June 2018 over Mainland China and the eight subregions.

3.2. Spatial Statistical Analysis of Error Features. To study the spatial characteristics of the RV06C, RV06UC, CDR, and BLD precipitation products over Mainland China, the continuous statistical indices *r*, RB, RMSE, and MAE are shown in Figure 5.

From Figures 5(a), 5(e), 5(i), and 5(m), it can be seen that the spatial distribution of *r* is positively related to the spatial distribution of average daily precipitation shown in Figure 2. According to Figures 5(a), 5(e), 5(i), and 5(m) and the average *r* values within Appendix E, *r* values for humid regions (CJ and HN) with low elevation and latitude are better than those of semi-humid regions (DB and HB). However, the humid YG subregion is an exception, and *r* values for RV06C, RV06UC, and BLD are significantly lower over the middle part of YG, especially for CDR. At the same time, values of *r* for semi-humid regions are larger than

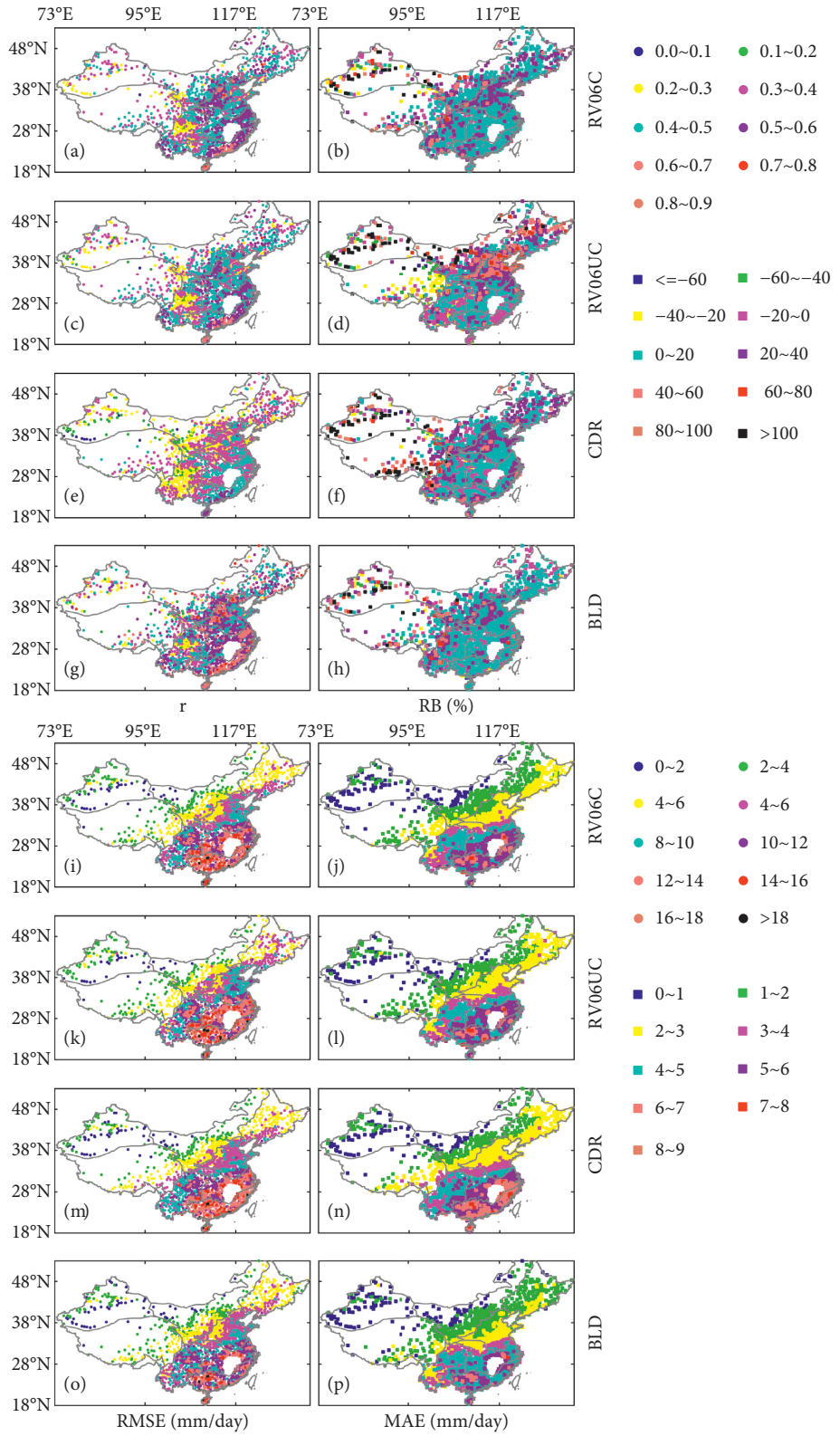

Figure 5: Spatial distributions of continuous statistical indices for the RV06C, RV06UC, CDR, and BLD product during the period from March 2014 to June 2018 over Mainland China. From left to right, the columns represent *r* RB (%), RMSE (mm/day), and MAE (mm/day).

those in arid and semi-arid regions (XJ and XB, respectively) with high elevation and latitude and those in the TP cold region with complex topography. In addition, BLD has the highest *r* and CDR shows the lowest *r* among the four SPPs. Note that this result is consistent with the prior analysis in Figure 4(a).

As for RBs, it can be seen that calibrated V06C improves the uncalibrated V06UC's overestimation over XJ, XB, DB, and HB. From the large number of yellow, green, and pink dots shown Figure 5(f), it can be clearly seen that V06UC shows a significant underestimation over TP. The four SPPs show remarkable overestimation for a number of gauge stations within XJ—see the many black dots within Figures 5(b), 5(f), 5(j), 5(n). In each subregion, SPPs not only show overestimation at some gauge stations, but also exhibit underestimation at other gauge stations. However, in general, positive biases are stronger and more prevalent than negative biases.

In terms of RMSE and MAE, the two IMERG products and CDR show similar spatial patterns. In general, BLD performs better than the other three SPPs according to Figure 5.

Variation in the values of r, RB, RMSE, and MAE metrics calculated for the RV06C, RV06UC, CDR, and BLD product is summarized by the boxplots in Figure 6.

Compared with RV06UC, RV06C shows considerable improvements in r. In terms of variation in the estimation of precipitation accumulations, RV06C performs better than RV06UC over most regions (except for TP, YG, and HN), as witnessed by shorter box lengths of RB for RV06C in those regions (Figure 6(b)). As for RMSE and MAE, the performance of RV06C is better than RV06UC with lower RMSEs and MAEs over most regions (except for TP, YG, and HN). From the above discussion, gauge calibration improves the overall performance of the uncalibrated RV06UC product.

All the four satellite-based products show high RB over XJ. The high discrepancies between SPPs and in situ observations may be due to sparse gauges, complex climate, and terrain characteristics that can result in high uncertainties in the evaluation of the SPPs at regional scales.

Compared with the other three SPPs, BLD shows the best performance with the highest r values (all regions) and the lowest RB (except for TP and YG), RMSE (except for arid XJ and TP cold region), and MAE (except for TP region). In addition, CDR shows the worst performance with the lowest r values and the highest MAEs (except for XJ region) among all the SPPs.

To further investigate the difference between the four SPPs, the spatial distributions of POD, FAR, and CSI metrics for each product are illustrated in Figure 7.

From Figure 7, one can clearly see that POD and SCI increase from the northwest and northeast to the southeast coast just like variation of precipitation amount over Mainland China. However, FAR has the reverse spatial tendency. In general, RV06C performs better than RV06UC over Mainland China in terms of POD, FAR, and SCI results. RV06UC POD results reveal that RV06UC misses some precipitation events over Mainland China, especially over TP. However, within northern part of HB, RV06UC detects more precipitation events. RV06C improves upon RV06UC's performance, especially over humid regions (YG, CJ, and HN) and within the TP cold region—perhaps due to the result of gauge adjustment. Compared with the two IMERG products, CDR obviously captures more precipitation events over Mainland China—particularly in the HB, CJ, DB, XB, and TP subregions and the northwest part of XJ. Likewise, BLD has the best POD among the four SPPs according to Figures 7(a), 7(d), 7(g), and 7(j).

Interestingly, the differences in FAR for the two IMERG products are not as obvious as those in POD, except for northern parts of the DB region and the northwestern part of HB. Moreover, RV06UC shows higher FAR values than RV06C over these two regions. CDR shows the worst FAR among the four satellite-based products according to Figures 7(b), 7(e), 7(h), and 7(k). At the same time, BLD achieves the smallest FAR over northern (XB and XJ) and eastern China (DB, HB, and CJ).

As with FAR, the differences in CSI are not obvious between the two IMERG products. However, RV06C appears slightly better than RV06UC according to Figures 7(c) and 7(f). Meanwhile, BLD has the best CSI performance, just like that of POD, among the four SPPs. However, CDR shows the worst CSI according to Figures 7(c), 7(f), 7(i), and 7(l). In the end, according to Figure 7, the worst POD, FAR, and CSI values occur over XJ region, which indicates that high systematic errors may be related to altitude effects and its arid climate.

The comparison of POD, FAR, and CSI for RV06C, RV06UC, CDR, and BLD over Mainland China and our eight subregions is shown in Figure 8. The four SPPs achieve good POD scores (more than 0.5613) over Mainland China and all eight subregions except for the XJ region and RV06UC over TP. Furthermore, the best PODs are found in HN and CJ (more than 0.6653). CDR and BLD demonstrate better PODs than the IMERG products over most regions (except for YG and HN). Regarding the two IMERG products, the scores of RV06C are higher than RV06UC over most regions except for HB (0.6354 vs. 0.6189 over Mainland China, 0.4461 vs. 0.443 over XJ, 0.6232 vs. 0.5335 over TP, 0.5746 vs. 0.5613 over XB, 0.6059 vs. 0.5744 over YG, 0.6085 vs. 0.6067 over DB, 0.616 vs. 0.6223 over HB, 0.6733 vs. 0.6653 over CJ, and 0.7021 vs. 0.6815 over HN). Among the four satellite-based products, BLD shows the best performance with highest POD (0.7214 over China, 0.5062 over XJ, 0.6338 over XB, 0.7061 over YG, 0.6998 over DB, 0.6761 over HB, 0.7768 over CJ, and 0.801 over HN) except for TP. These results are consistent with the categorical metric results shown in Figure 7.

The FAR values for the four SPPs are higher than 0.3814 in all regions. CDR has the highest FARs over all regions (0.6136 over Mainland China, 0.7618 over XJ, 0.5926 over TP, 0.6788 over XB, 0.56 over YG, 0.6613 over DB, 0.7122 over HB, 0.5748 over CJ, and 0.4859 over HN) among the four satellite-based products, while BLD shows the lowest FARs (0.4462 over Mainland China, 0.6204 over XJ, 0.5161 over XB, 0.4505 over YG, 0.4584 over DB, 0.5039 over HB, 0.3987 over CJ, and 0.3814 over HN) except those for TP. Compared with RV06UC, RV06C has slightly better FARs (0.4924 vs. 0.4966 over China, 0.6825 vs. 0.7062 over XJ, 0.5528 vs. 0.5596 over XB, 0.5554 vs. 0.574 over DB, 0.5715 vs. 0.5908 over HB, and 0.4602 vs. 0.4611 over XJ) over most regions.

With regard to CSI, all four SPPs have low CSIs (less than 0.5362) in all regions. As with FAR results, CDR has the

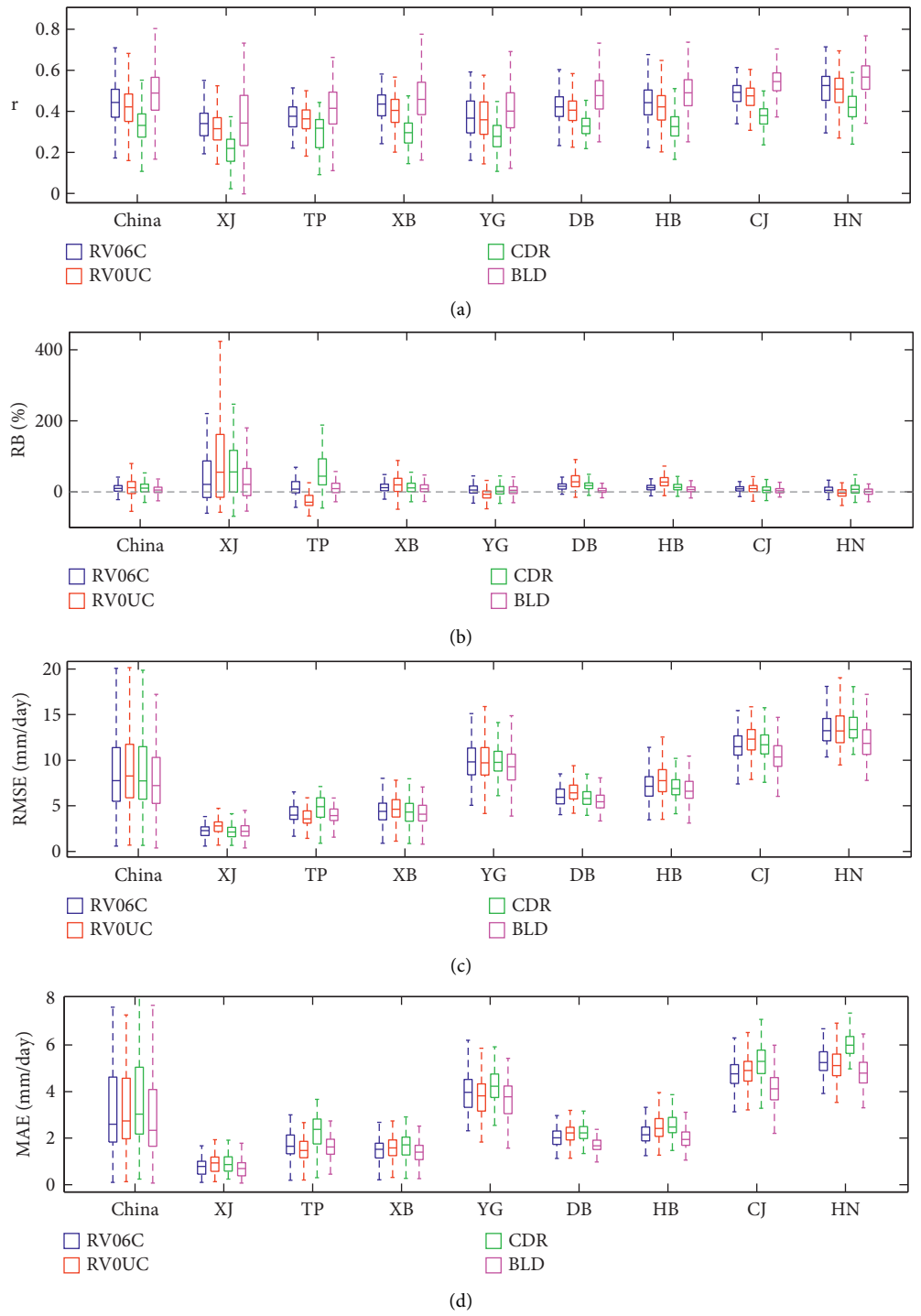

Figure 6: Boxplots of (a) correlation coefficient (r), (b) relative bias (RB), (c) RMSE, and (d) MAE for daily precipitation estimates from RV06C, RV06UC, CDR, and BLD during the period from March 2014 to June 2018 over Mainland China and our eight subregions. The five lines from top to bottom for each box describe the maximum value, 75th percentile, 50th percentile, 25th percentile, and minimum value levels, respectively.

worst scores in CSI (0.3205 over China, 0.1939 over XJ, 0.3407 over TP, 0.2678 over XB, 0.3409 over YG, 0.2893 over DB, 0.2518 over HB, 0.3542 over CJ, and 0.4164 over HN) among the RV06C, RV06UC, CDR, and BLD products. At the same time, BLD exhibits the highest CSI (0.4563 over China, 0.277 over XJ, 0.4234 over TP, 0.3782 over XB, 0.4472 over YG, 0.4395 over DB, 0.4008 over HB, 0.5128 over CJ, and 0.5362 over HN). RV06C performs better than RV06UC with higher CSI scores in each region according to Figure 8(c).

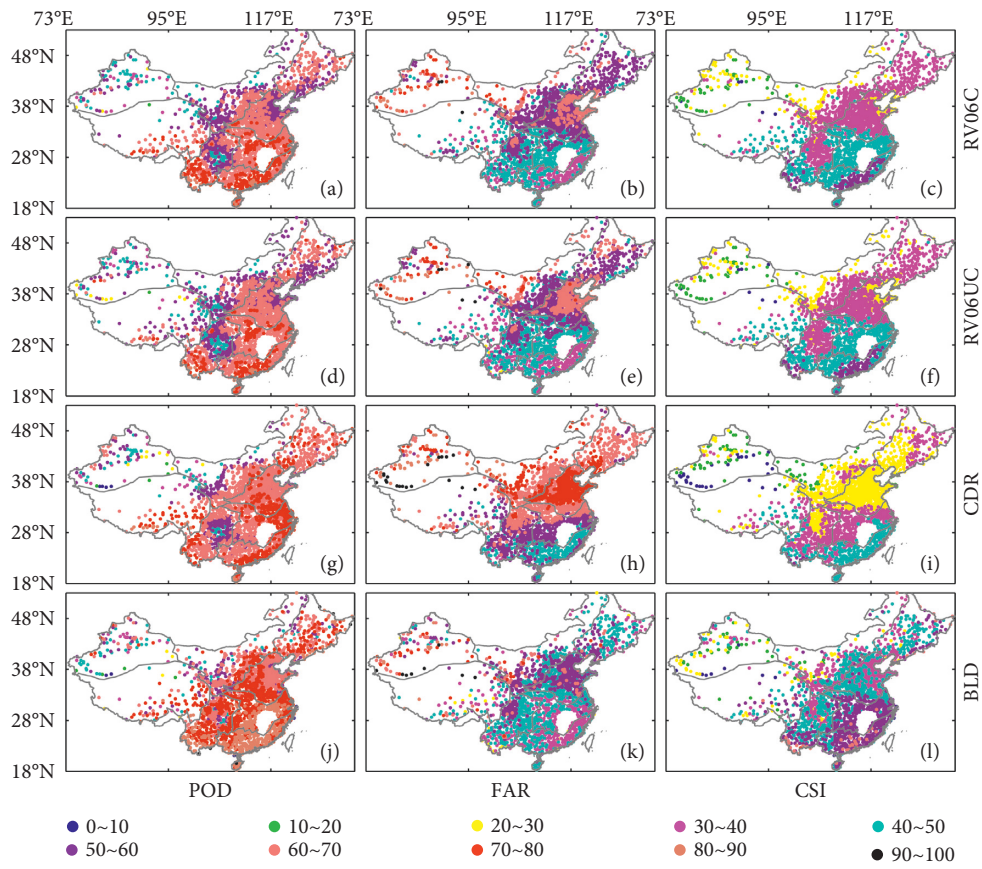

Figure 7: Spatial distribution of categorical statistical indices (POD, FAR, and CSI) for RV06C (first row), RV06UC (second row), CDR (third row), and BLD (fourth row), as compared to precipitation gauges' measurements derived from March 2014 and June 2018 over Mainland China.

3.3. Analysis of Error Components. To analyze temporal variations in precipitation error components during the period from March 2014 to June 2018, the time series of total bias and error components are shown in Figures 9–11. A 31-day running average was applied to the entire time series to reduce visual clutter. It can be seen that seasonality exists in each error component, especially in the winter and summer months. In general, lower values of total bias and error components are shown in the winter and higher ones in the summer over all regions. Such seasonality is mainly due to the uneven seasonal precipitation distribution over China. Simultaneously, the changing tendency of total bias and error-component curves also gives differences in different products and regions.

In terms of the two IMERG precipitation estimates, the changing tendency of missed error is highly similar over all regions with the exception of the TP. Over the TP, the amplitudes of missed errors for RV06C are slightly lower than those of RV06UC. The results indicate that the gauge adjustment of RV06C has little impact on MP event. At the same time, the changing tendencies of false error are highly similar over humid regions (YG, CJ, and HN) in Figures 10 and 11. However, when moving from a humid region to semi-humid, semi-arid, and arid regions, these differences increase slightly. Over the TP, an excessive number of MP events and large negative hit bias result in RV06UC's underestimation of total precipitation. At the same time, for RV06C, the most outstanding feature is the decrease of amplitude in hit bias and the upward adjustments for total bias according to Figures 9(i) and 9(j). Furthermore, the adjustments in warm months are larger than those in cold months. However, when gauge adjustments correct hit bias and MP of RV06C, they also elevate the FP rate of RV06C. As a result, RV06C still has a high total bias over the TP. Over XJ, the outstanding feature is the decrease of amplitude in false error and downward adjustments for total bias and hit bias in Figures 9(e) and 9(f). Furthermore, almost over all regions, compared with hit bias and negative missed errors, the positive false errors have a larger impact on the total biases of RV06C and RV06UC. The negative missed errors and positive false errors show very similar seasonal variability. In fact, they are mirror-symmetric in a way that they could partially offset each other. However, the season amplitude of the false errors is somewhat than that of the missed errors. Therefore, the total bias is generally positive. According to the above discussion and the description in Figures 9–11, we can see that RV06C improves upon the performance of precipitation of RV06UC over Mainland China, especially over XJ and TP.

Compared with the two IMERG products, the proportion of hit bias for CDR is larger almost in all regions. Meanwhile, the hit bias of CDR is generally negative over

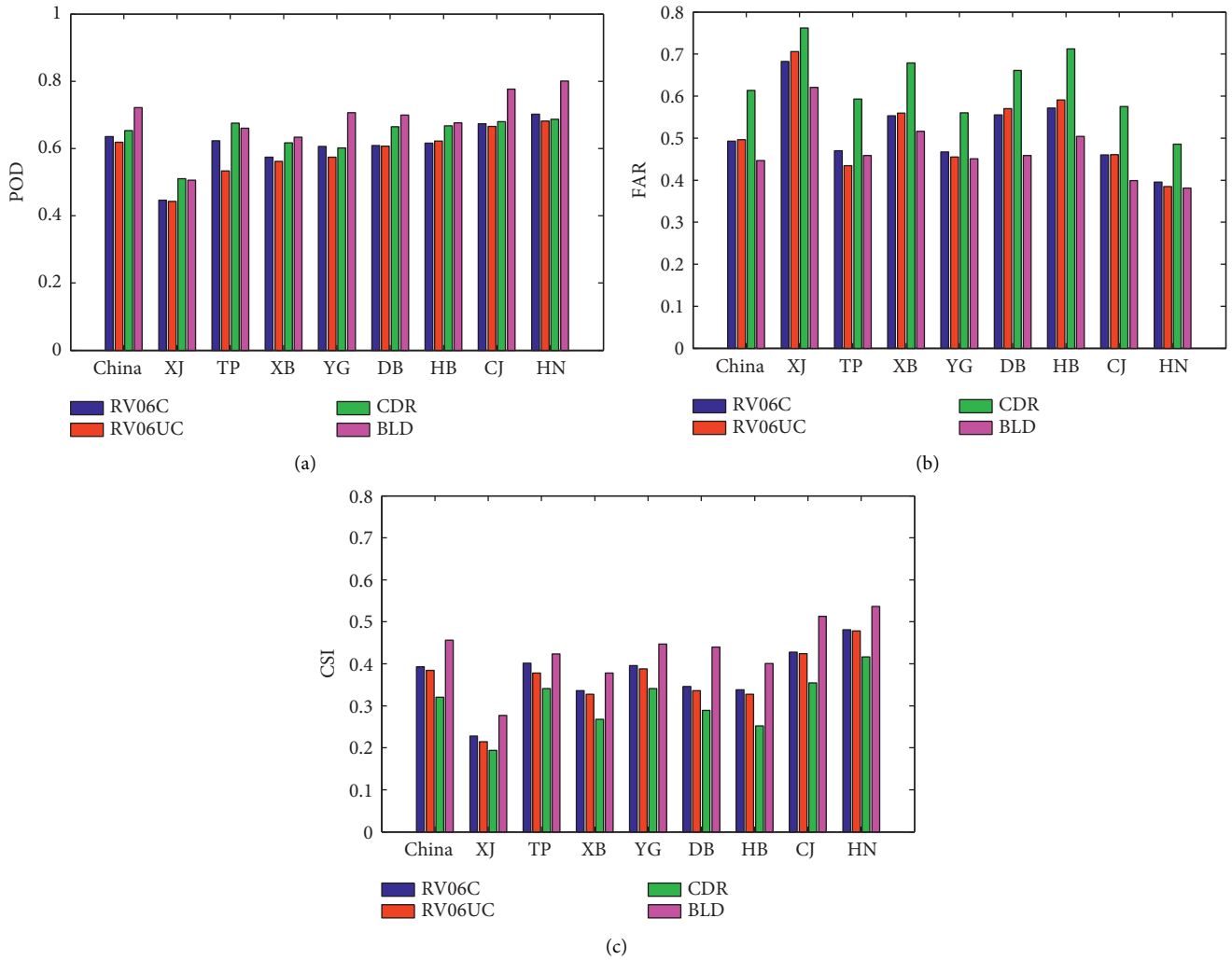

Figure 8: Categorical statistical indices: (a) POD, (b) FAR, and (c) CSI of daily precipitation for RV06C, RV06UC, CDR, and BLD satellite-based products compared to precipitation gauges over Mainland China and its eight subregions from March 2014 and June 2018.

most regions except for the TP, particularly in summer (rain season), which is not the same as the two IMERG precipitation estimates. Moreover, the amplitudes of FP increase over most regions (except for XJ), especially over the TP where the proportions of hit bias and positive false error of CDR increase substantially, particularly during summer. Meanwhile, the higher FP error and positive hit bias for CDR lead to a serious overestimation of precipitation. A similar result can be seen in Figure 4(b). However, the seasonal amplitude of MP tends to be slightly smaller over China and semi-humid subregions (DB and HB). As described above and observed in Figure 9(c), CDR shows the worst performance among all the precipitation products with the highest false error, hit bias, and total bias. In the end, its excessive FP rate may cause a problem for its application to hydrological forecasting.

As for BLD, compared with the other three satellite-based products, it seasonal amplitude in MP is slightly lower in Mainland China and most of our regions of interest (i.e., TP, XB, YG, HB, CJ, and HN). At the same time, BLD shows the best performance in terms of the smallest total bias over most regions—including TP, DB, HB, CJ, and HN (see Figures 9(l), 10(l), 11(d), 11(h), and 11(l)). Generally speaking, in comparison with the other three SPPs, BLD has lower seasonality amplitude of false error and missed error over China (Figure 9(d)), which substantially improves the error structure of the BLD output. However, the proportion of hit bias increases a little. Benefiting from the mutual offset of error components, the total bias of BLD is generally the lowest over Mainland China. At the same time, from the time series of false errors, missed errors, and total bias, it can be seen that the BLD has the best performance among the four SPPs over China.

3.4. Intensity Distribution Analysis of Error Components. Previous studies have shown that the errors of SPPs are closely related to precipitation intensity [33, 58]. To further explore the features of the error components of the four SPPs, the daily intensity distributions of total, hit, and MP, together with the FP events over Mainland China and our eight subregions for all summer and winter seasons (from

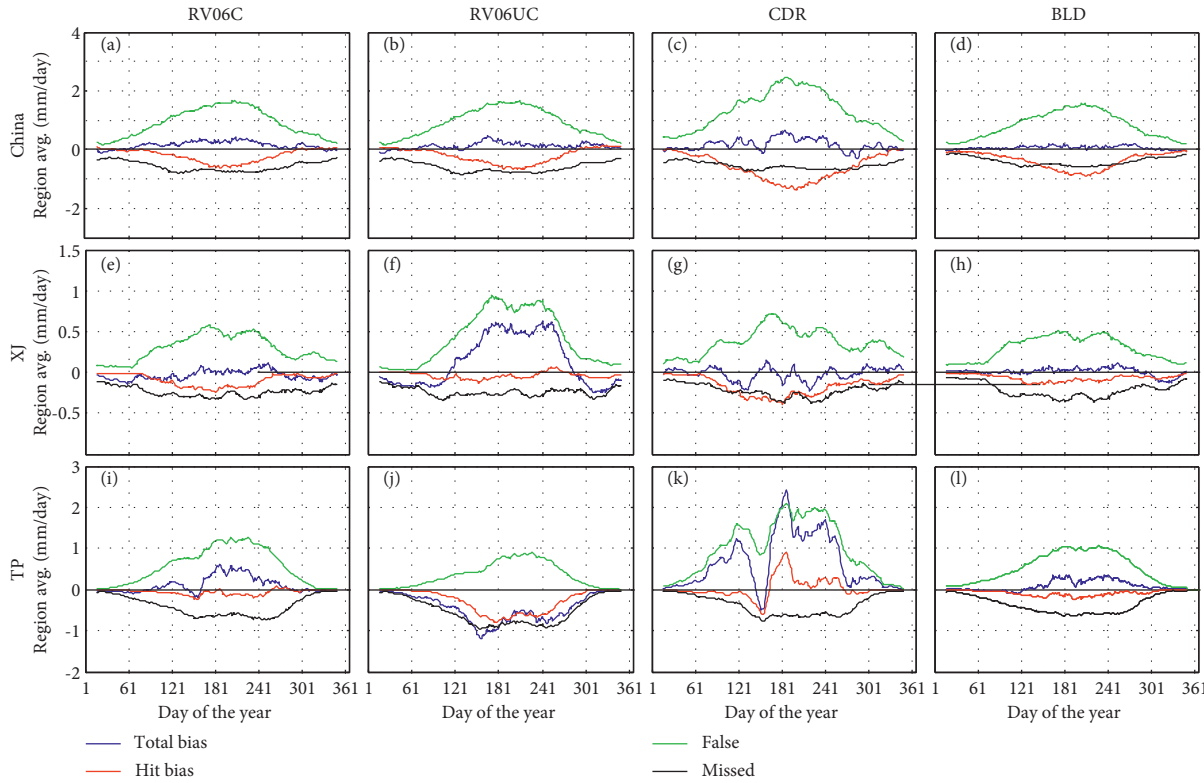

Figure 9: Regionally averaged time series of the total bias and error components for RV06C, RV06UC, CDR, and BLD during the study period from March 2014 to June 2018 over Mainland China and XJ and TP subregions. A 31-day moving average is utilized to each average daily precipitation time series to reduce visual cluttering.

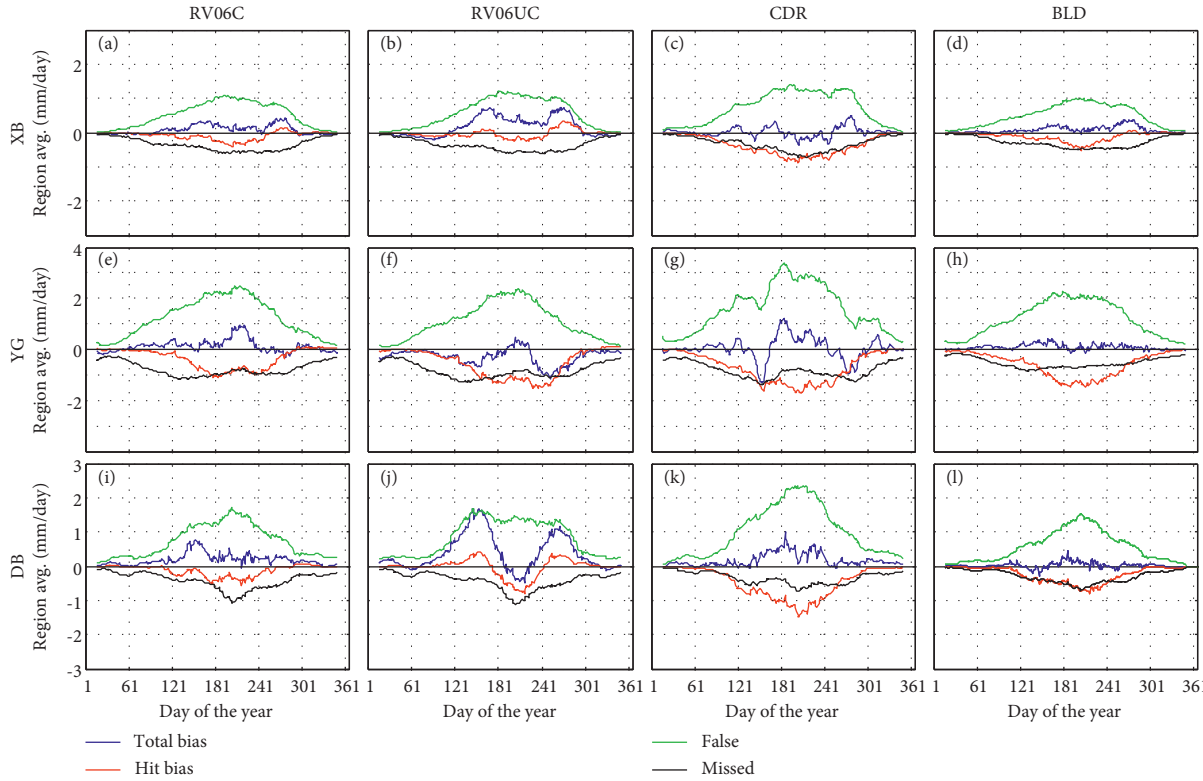

Figure 10: Same as Figure 9 except for the XB, YG, and DB subregions.

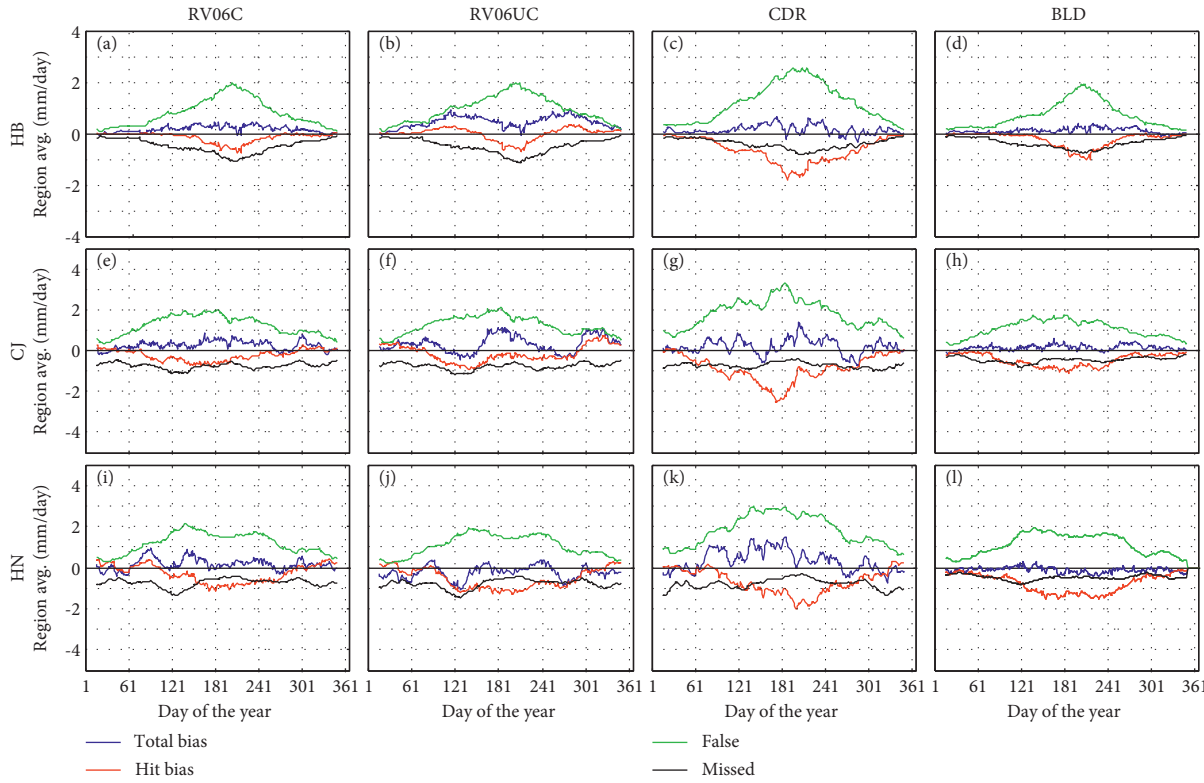

Figure 11: Same as Figure 10 except for the HB, CJ, and HN subregions.

March 2014 to June 2018), are shown in Figures 12–14 for summer seasons and Figures 15–17 for winter seasons. Here, it should be noted that a threshold of 1 mm/day is adopted to determine rain/no rain for any given day when computing the intensity distribution of error components. Since the intensity distributions are closer to lognormal, the logarithmic scale was used to bin precipitation rates across the range of 1–256 mm/day on the x-axis. The values on the y-axis stand for precipitation accumulation for each bin, which is obtained from the total days in the corresponding season.

For summer, over Mainland China, the two IMERG precipitation estimates generally show similar distribution of the total precipitation, with their differences being small, as shown in Figure 12(a). At the same time, in Figure 12(a), RV06C and RV06UC overestimate light precipitation and moderate precipitation events (<25 mm/day) and underestimate heavy precipitation events (>42 mm/day). However, RV06UC is closer to observations than RV06C at precipitation rates between 8 and 25 mm/day and at precipitation rates greater than 64 mm/day. However, for precipitation rates from 30 to 64 mm/day, RV06C is closer to the gauge observation than RV06UC. For BLD and CDR, compared with the two IMERG products, the underestimation of heavy precipitation (precipitation rate more than 42 mm/day) and the overestimation of light and moderate precipitation (precipitation rate less than 30 mm/day) become more pronounced (Figure 12(a)). Furthermore, the curve of total precipitation of CDR is farther from the rain-gauge-based reference curve (Figure 12(a)). The proportion of the MP is relatively small (Figure 12(c)). Compared with CDR, BLD has less MP events, while the two IMERG products show more MP events. Similar results can be seen in Section 3.3. The FP rate of the four satellite-based precipitation estimates is larger than MP rate. Meanwhile, CDR has a wide distribution of FP, concentrating at precipitation rates less than 42 mm/day (Figure 12(d)). RV06C, RV06UC, and BLD have the extreme similar distributions of selected s. Meanwhile, BLD looks slightly better than the two IMERG products, especially at precipitation rates more than 32 mm/day. The results are consistent with the above analysis in Section 3.3.

The performances of hit, false, missed, and total precipitation metrics for SPPs show remarkable regional differences. Over the TP (Figures 12(i)–12(l)), the curve of total precipitation for RV06C is much closer to that of rain-gauge reference curve than RV06UC. Furthermore, the upward adjustments are concentrated at precipitation rates from 4 mm/day to 64 mm/day (Figure 12(j)). Meanwhile, MP rates decrease across precipitation rates. However, the unfavorable overcorrection of FP is found at all precipitation rates. In general, the calibration process used in RV06C is effective over the TP (Figure 12(i)). CDR overestimates total precipitation at almost all precipitation rates (Figure 12(i)). Likewise, BLD shows relatively good performance in terms of total, hit, and missed precipitation (Figures 12(i)–12(k)). Over XJ (Figures 12(e)–12(h)), RV06C is successful at correcting total precipitation for light rain with precipitation rates ranges from 1.3 mm/day to 10 mm/day and FP at all precipitation rates. The excessively downward correction in total precipitation is concentrated at precipitation rates from 16 mm/day to 105 mm/day. BLD shows the best

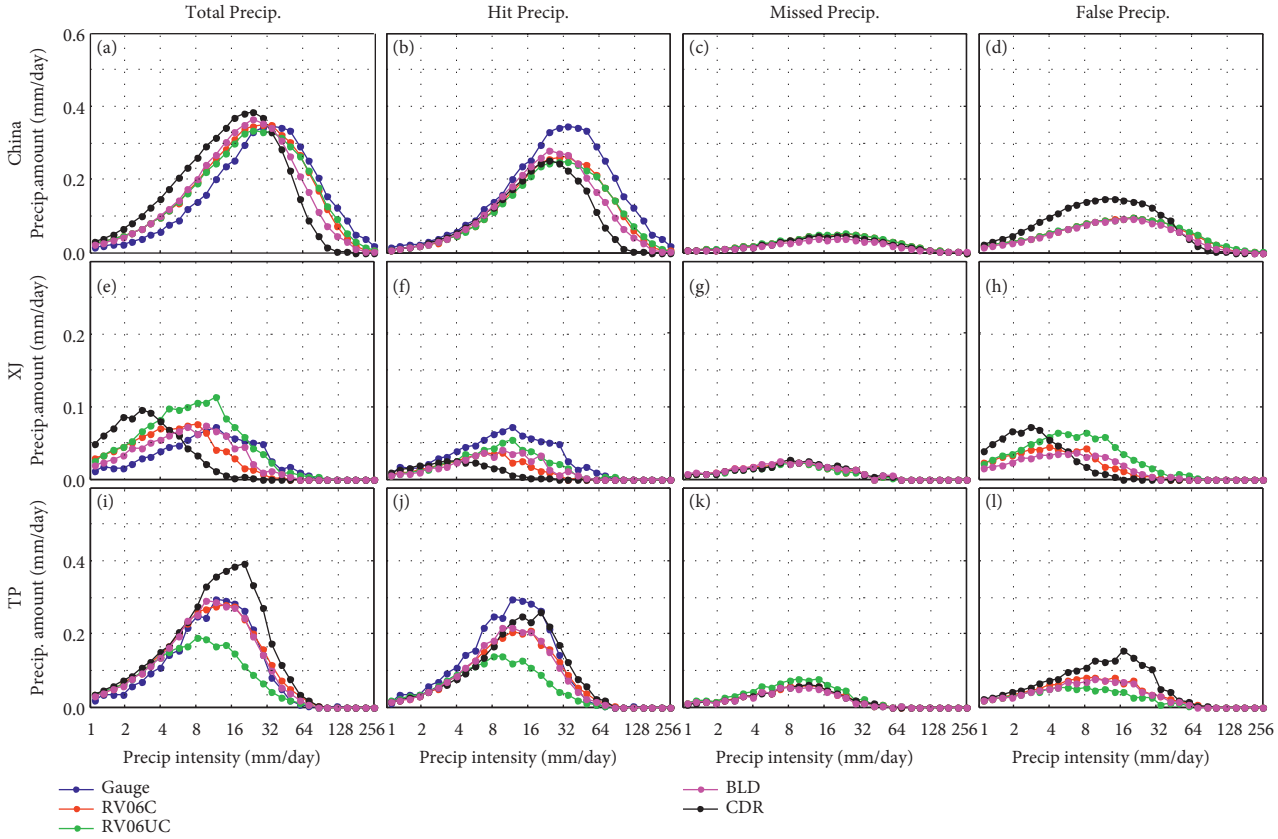

Figure 12: The daily intensity distribution of the total, hit, missed, and false precipitation summer metrics during the period from March 2014 to June 2018 over Mainland China and the XJ and TP subregions. The total precipitation of gauge (blue line) is also shown in the first two columns for comparison.

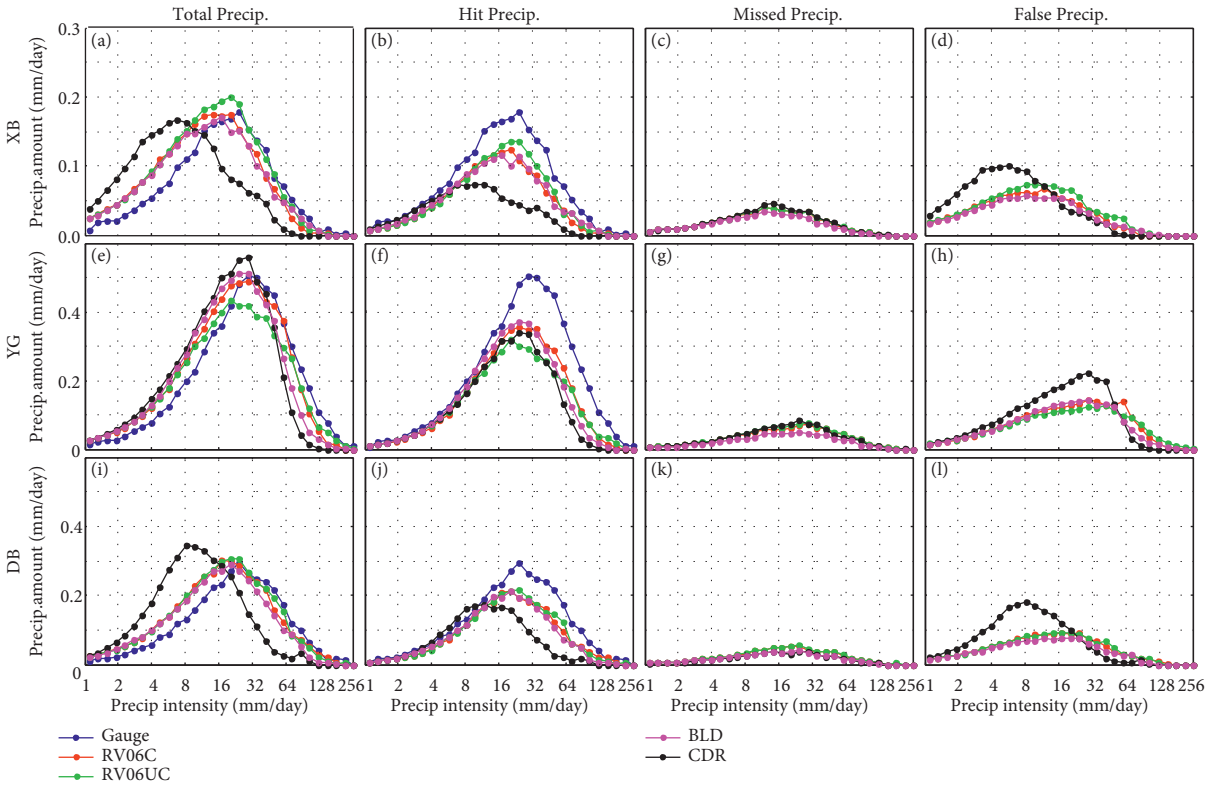

Figure 13: Same as Figure 12 except for the XB, YG, and DB subregions.

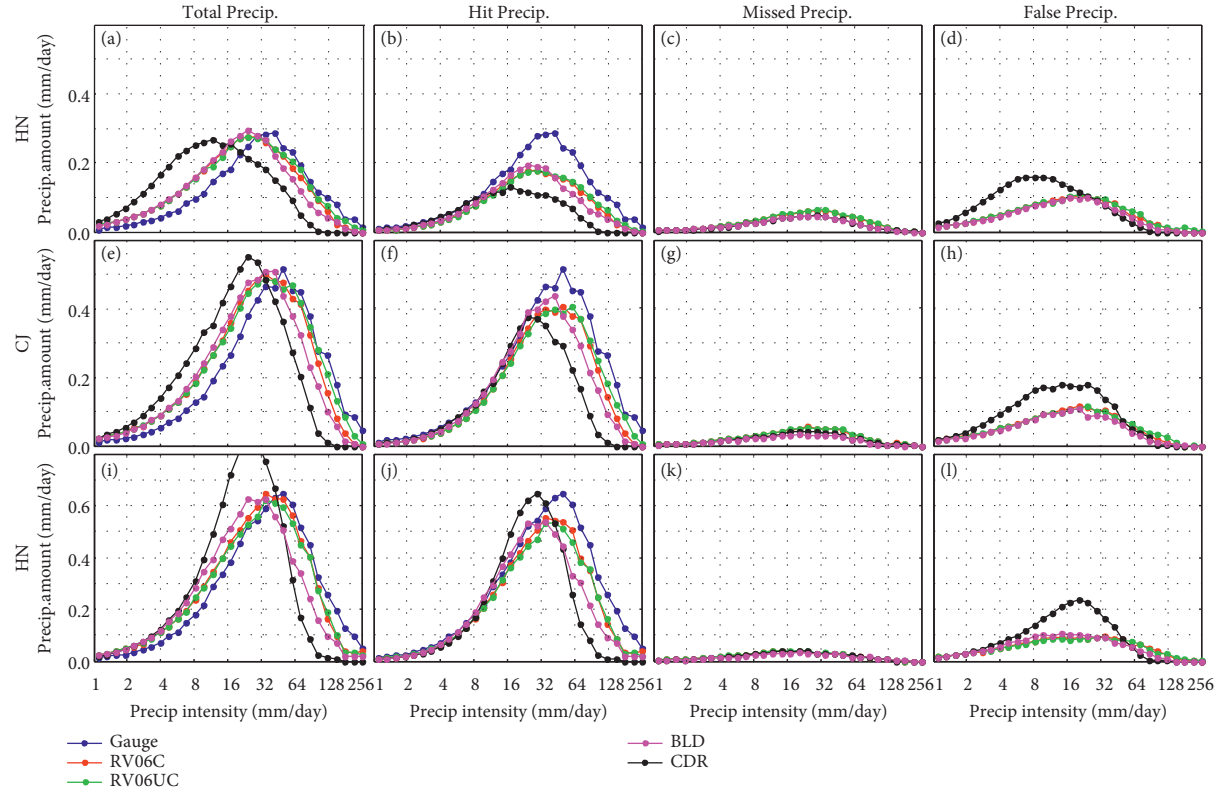

Figure 14: Same as Figure 12 except for the HB, CJ, and HN subregions.

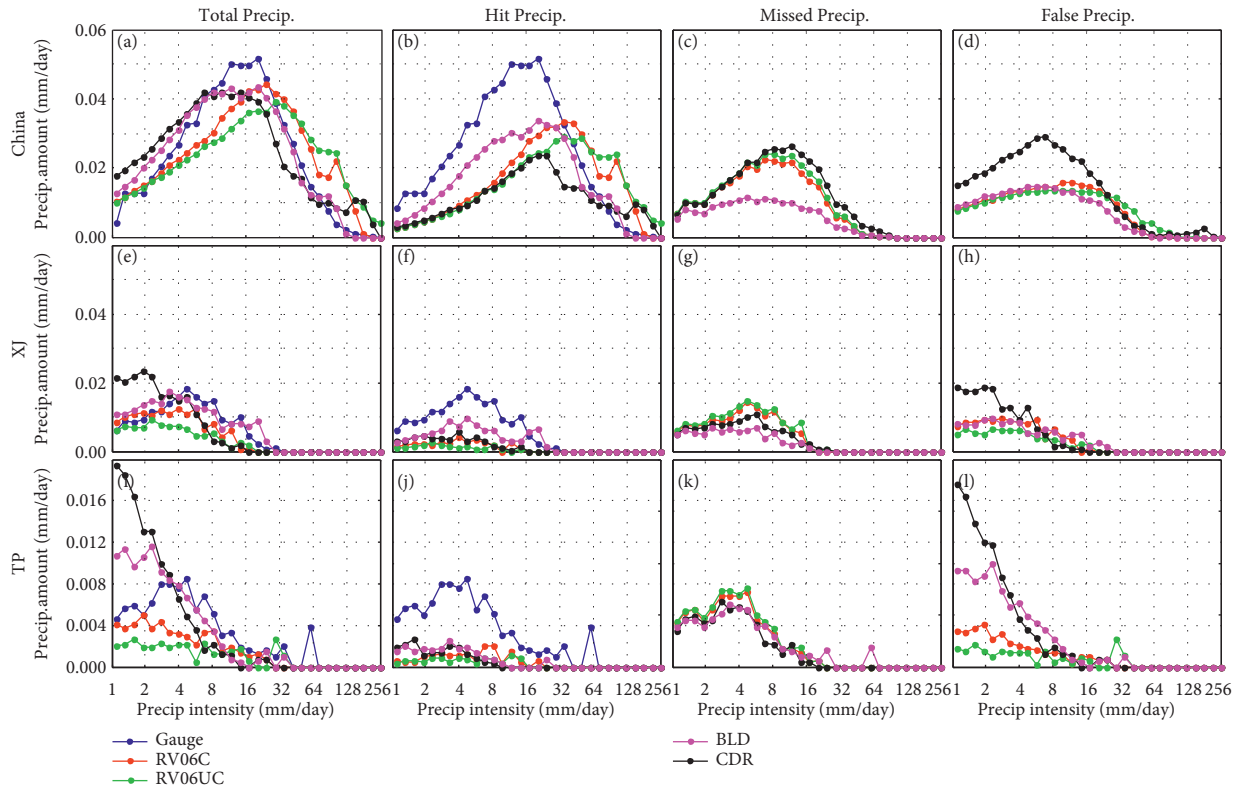

Figure 15: The daily intensity distribution of the total, hit, missed, and FP in winters for the period from March 2014 to June 2018 over Mainland China and XJ and TP subregions. The total precipitation of gauge (blue line) is also shown in the first two columns for comparison.

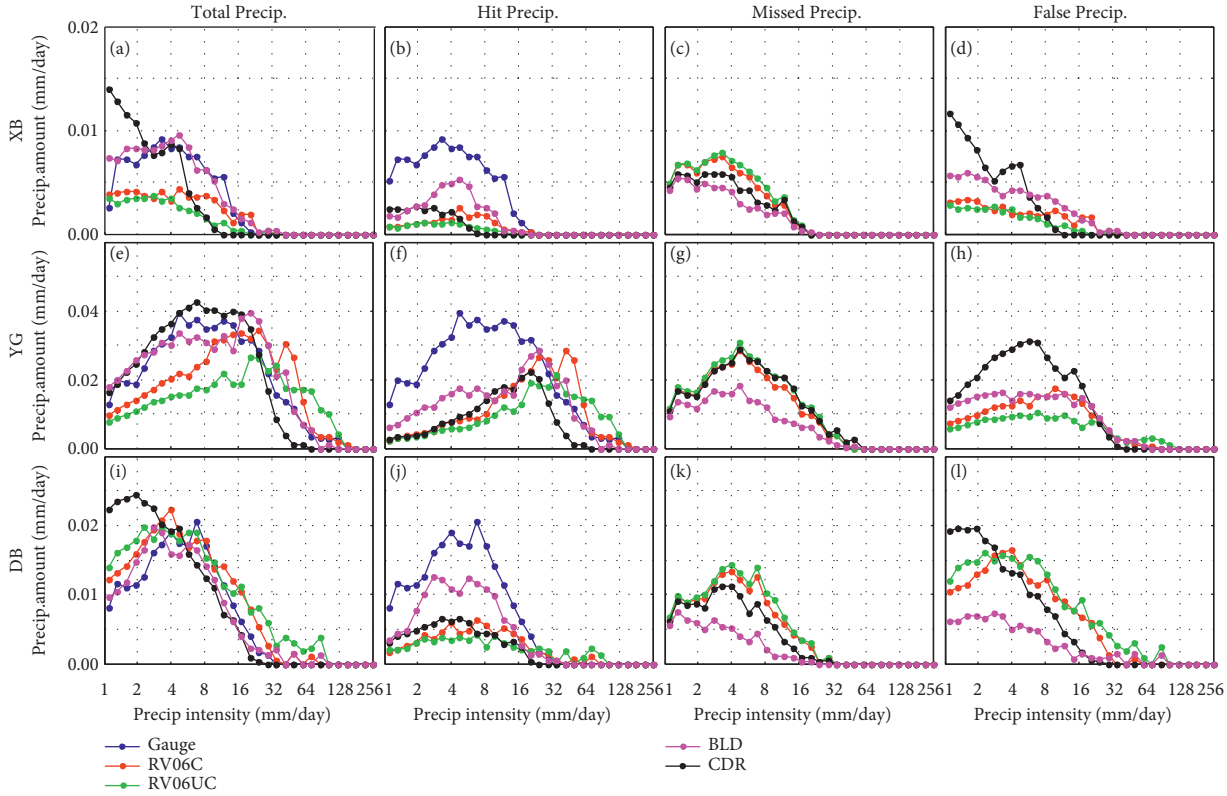

Figure 16: Same as Figure 15 except for the XB, YG, and DB subregions.

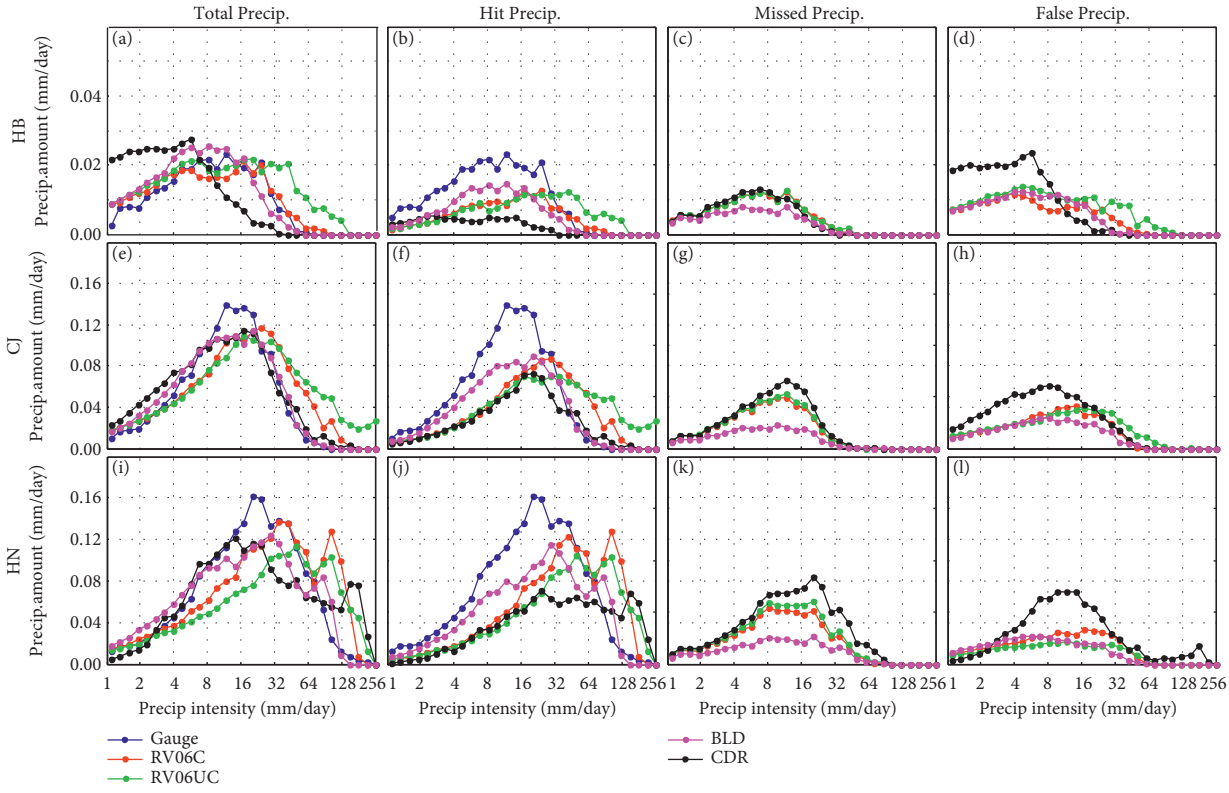

Figure 17: Same as Figure 15 except for the HB, CJ, and HN subregions.

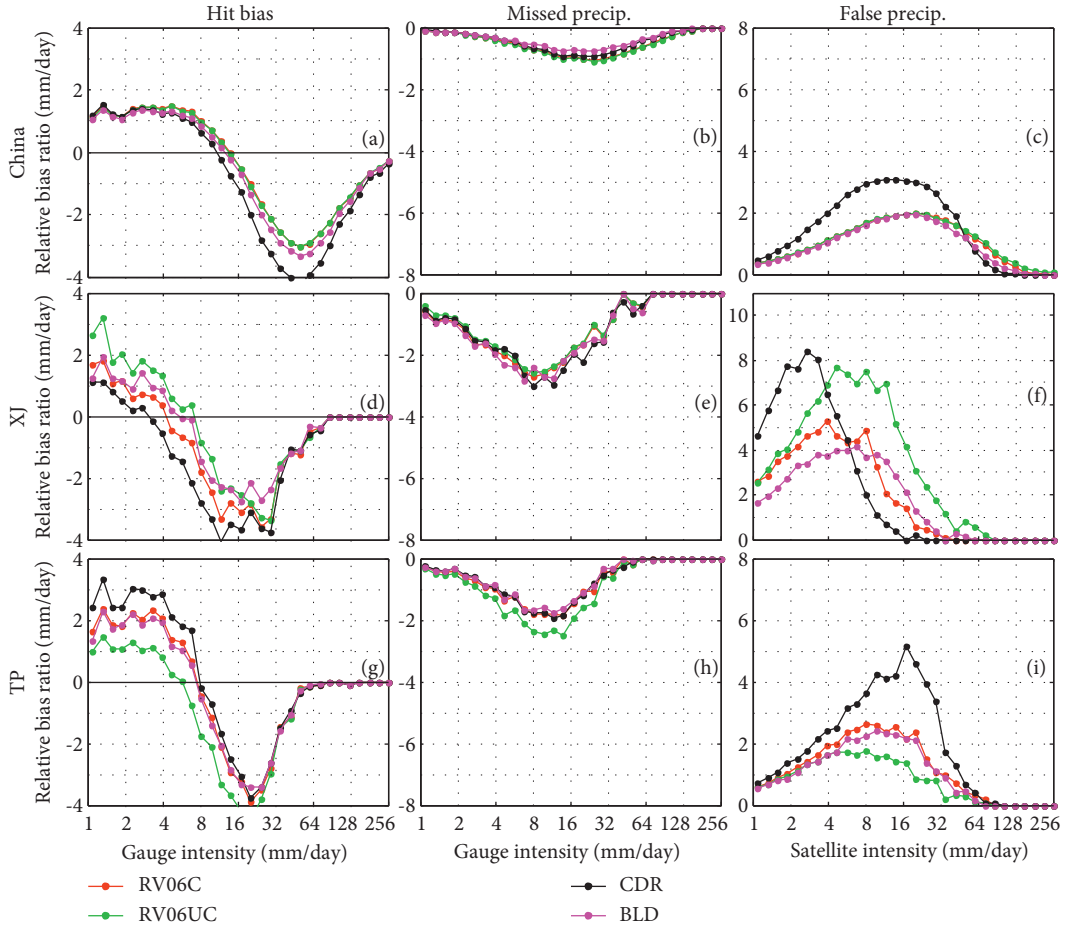

FIGURE 18: Intensity distribution of relative bias ratio for the error components of RV06C, RV06UC, CDR, and BLD during summers for the period from March 2014 to June 2018 over China and XJ and TP subregions.

performance in total precipitation at precipitation rates less than 21 mm/day and FP at precipitation rates less than 6 mm/day among the four satellite-based precipitation estimates. CDR's poor performance is mainly caused by excessive FP since the intensity distribution of FP looks like that of total precipitation, and the proportion of daily missed and hit precipitation is relatively small. Over XB, between two IMERG products, RV06C shows a downward adjustment in hit precipitation for precipitation rates above 12 mm/day and in FP for precipitation rates over 4 mm/day (Figures 13(b) and 13(d)). While, over YG, RV06C has an upward adjustment in hit precipitation for precipitation rates between 10 mm/day and 72 mm/day and in FP for precipitation rates between 8 mm/day and 72 mm/day (Figures 13(f) and 13(h)). At the same time, there is almost no adjustment in MP. Over the semi-humid subregions (HB and DB) and humid subregions (CJ and HN), RV06C and RV06UC share similar curve tendencies of total, hit, missed, and FP (Figures 13 and 14).

Impressively, over most subregions (except for TP and YG), CDR, compared with other three SPPs, generally shows relatively more precipitation during light or moderate precipitation and has obviously less precipitation in heavy precipitation cases in the hit scenario (the second column of Figures 12–14). At the same time, the CDR and the other three satellite-based precipitation products have three intersection points, respectively. These points are very close, and they all change with climatic variation. Moreover, the points gradually increase for the wetter and wetter climate regions (from about 4 mm/day over arid XJ to about 6 mm/day over semi-arid XB, about 12 mm/day over semi-humid HB and DB, and eventually about 32 mm/day over humid CJ and HN, respectively), which may be related to the uneven precipitation distribution over China. Meanwhile, a similar situation occurs with regard to FP (the fourth column of Figures 12–14) over most subregions (except for the TP cold region). Over these subregions, an underestimation of heavy rain in total precipitation (see the first column of Figures 12–14) is attributed to the less precipitation in the heavy rain in CDR hit and false scenarios (see the second and fourth columns of Figures 12–14). At the same time, more precipitation in the light or moderate rain in CDR hit and false scenarios result in an overestimation of light and moderate rain categories in total precipitation.

Similar to summer results, over Mainland China (Figure 15(a)), the difference in total precipitation of the two IMERG precipitation estimates is relatively small. Meanwhile, both RV06C and RV06UC underestimate light precipitation and moderate precipitation events at precipitation rate between 2.7 mm/day and 24.4 mm/day and overestimate heavy precipitation events for precipitation rates larger than

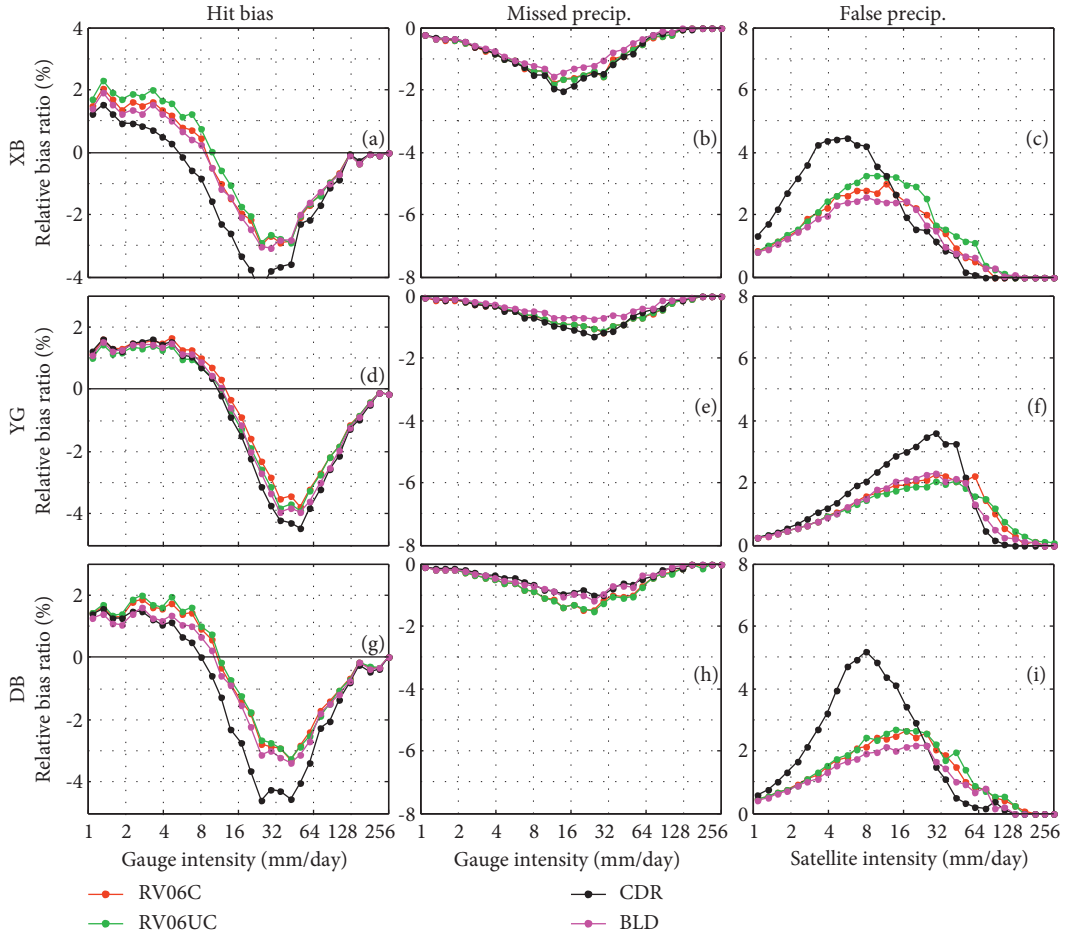

Figure 19: Same as Figure 18 except for the XB, YG, and DB subregions.

29.3 mm/day. At the same time, RV06C is closer to observations than RV06UC at precipitation rates of more than 2.7 mm/day (except for individual situation). However, the situation with regard to total precipitation for CDR and BLD is different from that of the two IMERG products. CDR and BLD show overestimation at light precipitation with precipitation rate below 5.7 mm/day and underestimation at moderate precipitation and heavy rain with precipitation rates from 8.2 mm/day to 73 mm/day. Furthermore, it is generally true that the curve of total precipitation for BLD is closer to the rain-gauge reference curve than that for CDR. For hit precipitation (Figure 15(b)), compared with BLD, the other three SPPs show less hit precipitation at precipitation rates below 24.4 mm/day. However, the two IMERG products have more hit precipitation than BLD at precipitation rates greater than 35 mm/day.

MP (Figure 15(c)) accounts for a larger proportion of total error in winter than in summer. During the winter, the MP of BLD is much lower than that of the other three satellite-based products. Furthermore, CDR has the most MP with precipitation rates more than 4.7 mm/day. From Figure 15(d), it can be seen that CDR has the highest FP rate when precipitation rates fall below 24.4 mm/day. The FP rates of RV06C, RV06UC, and BLD are all similar for precipitation rates less than 8 mm/day. However, when precipitation rates are greater than 11.8 mm/day, BLD shows the smallest FP rate among the four satellite-based precipitation estimates.

Over the arid XJ subregion, Figures 15(e)–15(h) show that the total, hit, missed, and FP rates fall within the range of 1 to 30 mm/day for the four SPPs. Except for individual situation, RV06UC has less hit precipitation at all precipitation rates (Figure 15(f)), and RV06C shows a slightly upward adjustment at most precipitation rates. Among the four SPPs, BLD has the highest hit precipitation rate at all precipitation rates. The two IMERG products have more MP than BLD and CDR. Furthermore, BLD exhibits the lowest MP rate at almost all precipitation rates (Figure 15(g)). As for FP, an unfavorable overcorrection was found in RV06C. CDR shows more FP for precipitation rates less than 4.7 mm/day. Over XJ, compared with the missed and FP, hit precipitation possesses relatively small proportion in winter (except for BLD). Over the TP cold region, the curves of hit, missed, false, and total precipitation show relatively little variation. The intensity distribution of total precipitation looks like that of FP, and the hit precipitation accounts for a relatively smaller proportion (Figures 15(i), 15(j), and 15(l)). All the four SPPs show more MP events s when precipitation rates are less than 8 mm/day (Figure 15(k)).

Over the semi-arid XB subregion (Figures 16(a)–16(d)), RV06C, RV06UC, and CDR show less hit precipitation in

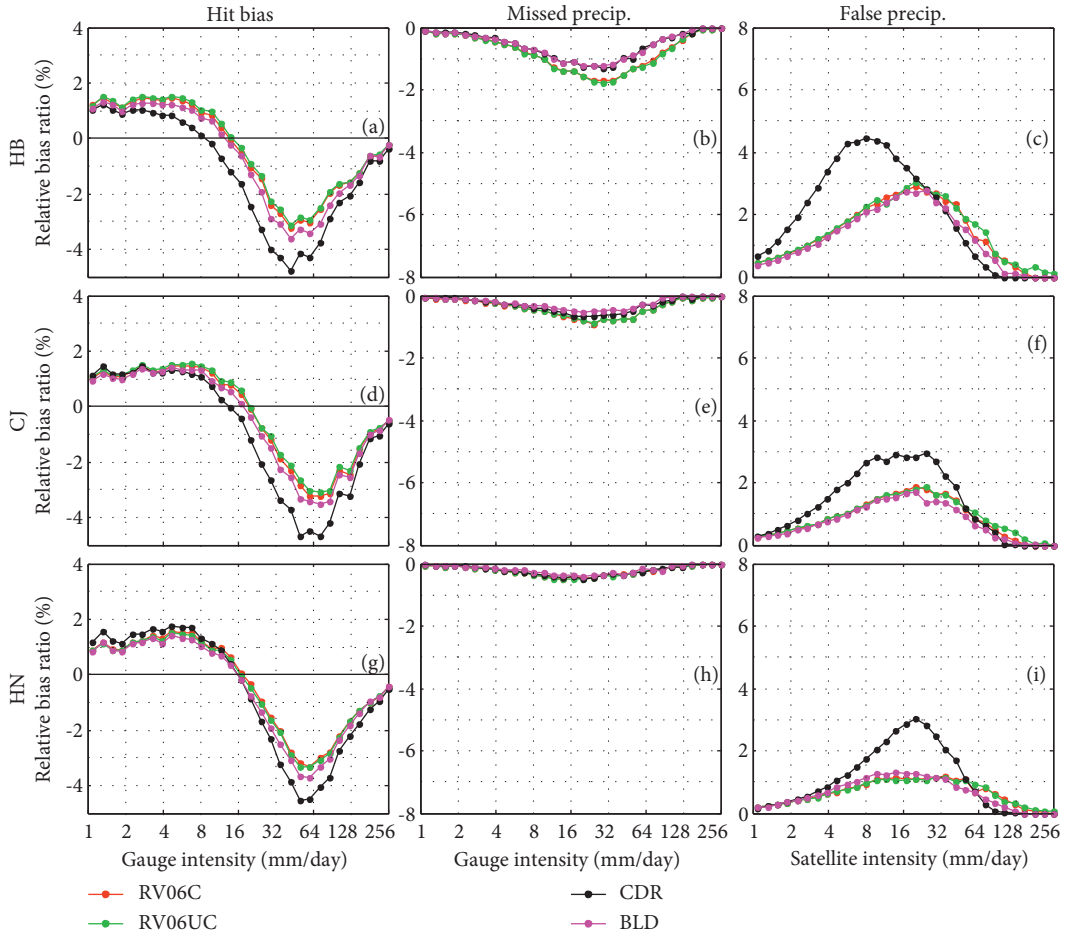

Figure 20: Same as Figure 18 except for the HB, CJ, and HN subregions.

comparison with their FP. For this reason, the intensity distribution of the total precipitation for the three satellite-based products is similar to that of FP, while BLD shows relatively more hit precipitation and less MP. Thus, the total precipitation of BLD is the closest to the reference curve among the four satellite-based products. However, compared with the two IMERG products, BLD shows more FP events at precipitation rates less than 16 mm/day. Over the humid YG (Figures 16(e)–16(h)) and HN (Figures 17(i)–17(l)) subregions, RV06C shows an upward adjustment in hit precipitation (with precipitation rates form 3.2 mm/day to 42 mm/day over YG and from 3.2 mm/day to 126 mm/day over HN, except for individual situation) and in FP (with precipitation rates between 1 mm/day and 24.4 mm/day over YG and from 1 mm/day to 35.1 mm/day over HN). At the same time, a slightly downward adjustment is found in MP events at precipitation rates less than 29.3 mm/day over YG (Figure 16(g)) and less than 87.4 mm/day over HN (Figure 17(k)). In general, the two IMERG products underestimate rates in the case of light or moderate precipitation and overestimate rates for heavy precipitation over the humid subregions (YG, CJ, and HN) in winter. For example, RV06C and RV06UC underestimate precipitation for precipitation rates from 3.3 mm/day to 20 mm/day and overestimate precipitation for precipitation rates larger than 24 mm/day (Figure 17(e)). Generally speaking, RV06C shows better performance than RV06UC over the YG, CJ, and HN subregions because RV06C has less MP events (Figure 16(g) and Figures 17(g) and 17(k)) and the intensity distribution of total precipitation for RV06C is relatively closer to gauged-based reference curve than that of RV06UC (Figure 16(e) and Figures 17(e) and 17(i)). Among the four SPPs, BLD has the least number of MP events over humid regions (YG, CJ, and HN), while CDR shows the most MP over CJ and HN. Furthermore, CDR exhibits relatively more FP events over the three humid subregions. Over the semi-humid DB subregion, the intensity distribution of hit precipitation for BLD is nearest to total precipitation of gauge observations at precipitation rates less than 14 mm/day (Figure 16(j)), and BLD has the least MP events for all precipitation rates (Figure 16(k)) and the least FP with precipitation rates less than 17 mm/day (Figure 16(l)) among the four SPPs. However, over the semi-humid HB subregions, As for the DB subregion, BLD does not show the same superiority over the other three precipitation products.

3.5. Relative Bias Ratio of Error Components. To further analyze the dependency of key error metrics on precipitation rate intensities, the intensity distribution of the relative bias

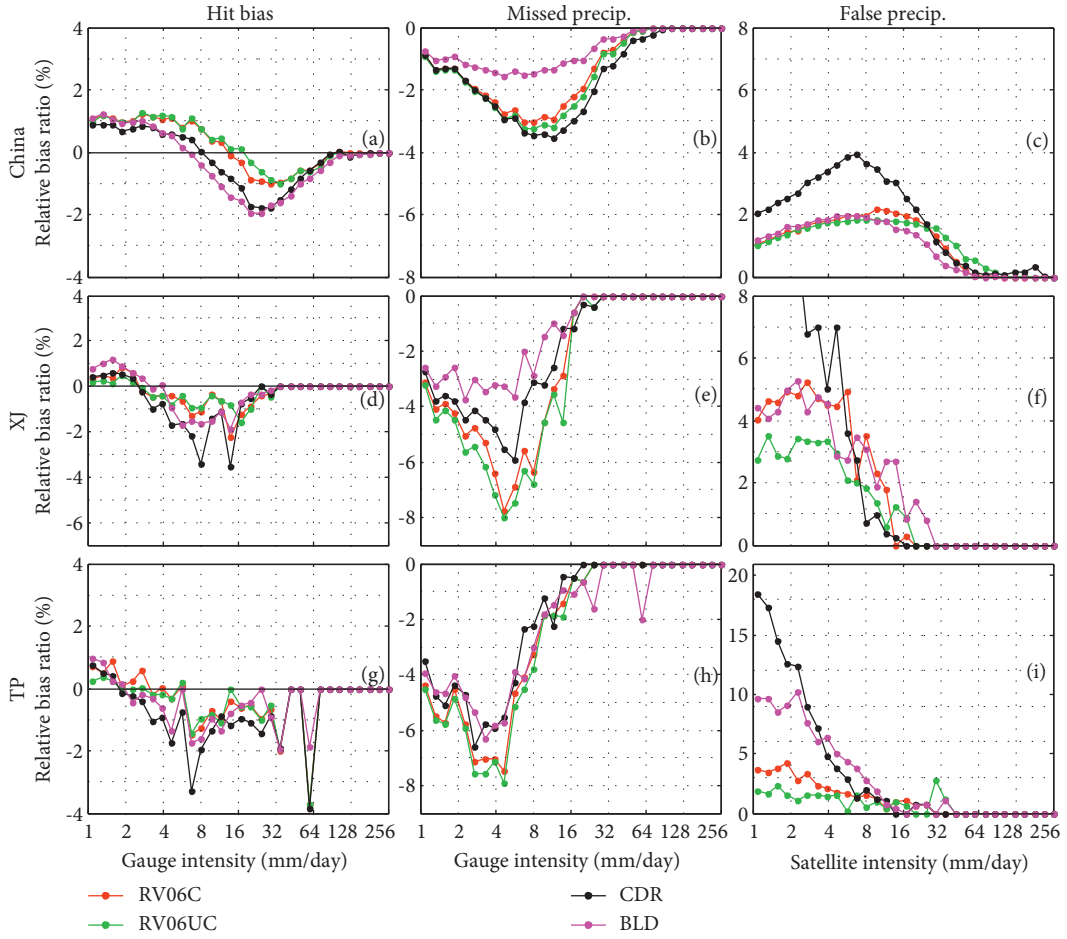

Figure 21: Same as Figure 18, but for winter seasons.

ratio for Mainland China and our eight subregions for all summer and winter seasons (from March 2014 to June 2018) is shown in Figures 18–20 for the summer season and Figures 21–23 for the winter season. Appendix F shows the relative bias ratio (RBR) for the hit bias (HB), negative hit bias (NHB), and positive hit bias (PHB).

The hit bias distributions of RV06C, RV06UC, CDR, and BLD all share a common error characteristic: overestimation at lower precipitation rates and underestimation at larger precipitation rates (the first column of Figures 18–23). This phenomenon is mainly caused by the nonunique relation between brightness temperature and surface precipitation. The satellite's observed brightness temperature derived from infrared (IR) or passive microwave (PMW) sensors reflects the combined effects of surface emission and evapotranspiration, not the surface precipitation rate. That is to say, the different combinations of precipitation profiles and surface background may produce the same surface precipitation rate. For this nonunique relation, light precipitation can be overestimated because the brightness temperature signatures of heavy precipitation are quite similar to those of light precipitation, and vice versa.

Over China, the largest contributions to the negative hit biases for the four SPPs are found at large precipitation rates (peak values at about 50.6 mm/day for summer in Figure 18(a) and 26.8 mm/day for winter in Figure 21(a)). The high rainy events gradually play an important role as climate gets progressively wetter. As a result, the peak values of contribution ratio for hit precipitation dynamically move to the larger precipitation rates. For example, during the summer, peak values are about 16 mm/day over the arid XJ subregion, 24.4 mm/day over semi-arid XB, 42.2 mm/day over semi-humid subregions (DB and HB), and approximately 64 mm/day over more humid subregions (HN, CJ, and YG). The curves exhibit volatility over XJ and TP, especially for winter (Figures 21(d)–21(i)). The result may be related to the following: (1) the complex topography and the short-lived convective storms or warm rain processes pose a challenge for remote sensing satellite rainfall observations; (2) rain events and rain accumulation are relatively less; (3) gauges are few over the two regions.

Generally, the difference of error components for the four SPPs in winter is relatively obvious than that in summer. At the same time, the most dominant difference occurs over XJ and TP. For example, for the two IMERG products, the gauge adjustments of RV06C lower the curve of relative bias ratio at light and moderate precipitation (precipitation rate less than 24.4 mm/day) over arid XJ (Figure 18(d)). Meanwhile, RV06C decreases the hit bias ratio at precipitation rates less than 4 mm/day and increases

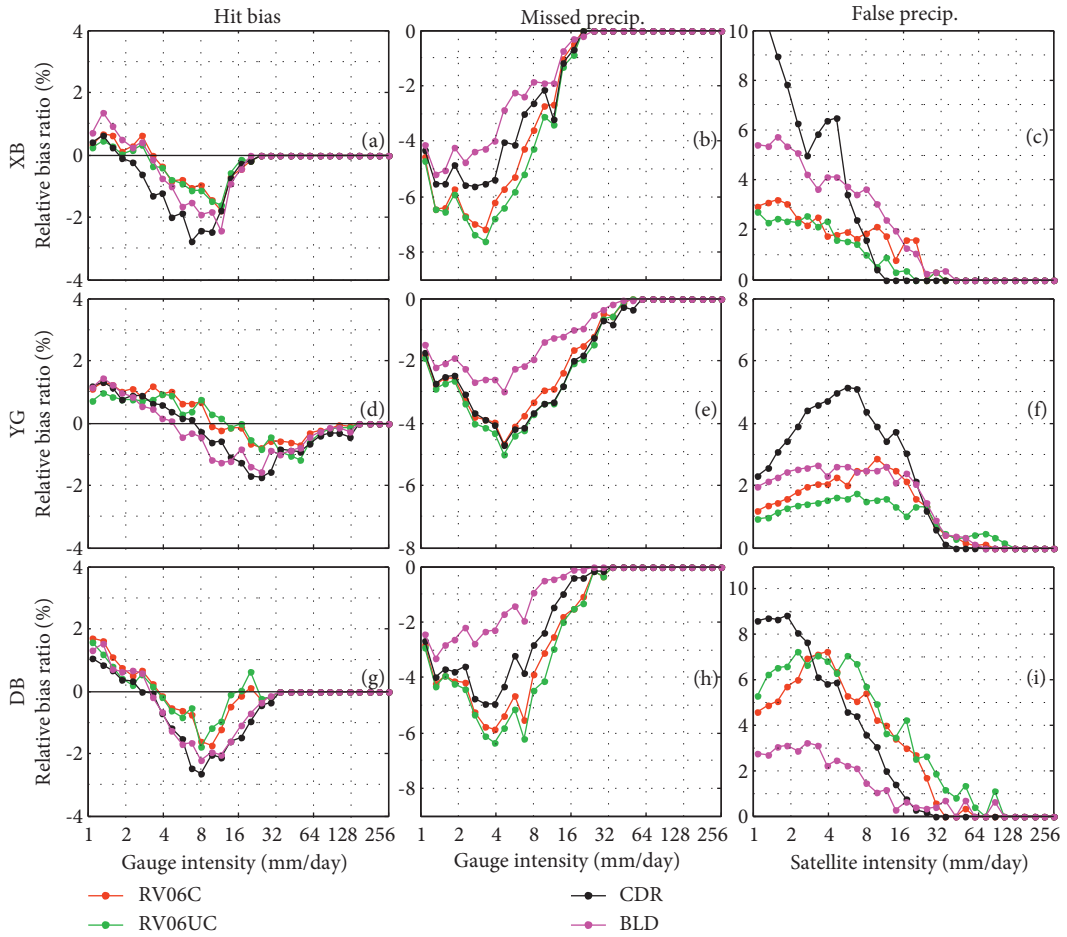

Figure 22: Same as Figure 19, but for winter seasons.

the hit bias ratio at precipitation rates between 4.7 mm/day and 24.4 mm/day. Over TP cold region, the reverse situation appears. The gauge adjustments of RV06C raise the curve of relative bias ratio for precipitation rates less than 29.3 mm/day (Figure 18(g)). Moreover, RV06C increases the hit bias ratio for precipitation rates less than 6.8 mm/day and decreases the hit bias ratio for precipitation rates from 8.2 mm/day to 29.3 mm/day. Compared with the intensity distribution of relative bias ratio, the frequently used intensity distributions of precipitation amount cannot show the actual variation of the bias ratio before and after the calibration. For example, after the gauge adjustment corrections, some small rain events may be adjusted to larger ones at higher precipitation rates (Figure 12(j)). However, the contribution of these adjusted small rain events to total bias is clearly shown in Figure 18(g).

With regard to MP, except for the TP region, the two IMERG products share extremely similar intensity distribution of relative bias ratio during the summer season (see the second columns of Figures 18–20). Over the TP subregion, RV06C decreases the amplitude of intensity distribution of relative bias ratio for MP events, while RV06C slightly improves RV06UC's MP over most regions except HB in winter (the second columns of Figures 21–23). This result indicates that the gauge adjustments have little influence on missed rain events in the GPM retrieval process (during the summer). However, they play a relatively active role during missed rainy events in wintertime.

Figures 18–23 show that the contribution from MP to the total bias exhibits regional and seasonal dependencies. In summer, the highest contribution of MP is that over arid XJ subregion, followed by the semi-arid XB region. The contributions of MP over TP cold region and semi-humid region (HB and DB) are a bit smaller, ranking, respectively, the third and fourth. Additionally, the contribution of humid region (YG, CJ, and HN) comes last. In winter, the largest contributions of MP occur over the XJ, XB, and TP subregions, followed by those over the HB and DB subregions. Moreover, the contribution of humid CJ and HN regions is the smallest. However, in winter, the humid YG region is an exception. Generally speaking, the contribution of MP seems to be lower over wetter regions. For the same climate region, the contribution of MP is obviously lower in summertime than during the winter. These results may be due to several factors: (1) wetter regions have more rainfall and relatively flatter topography than direr regions; (2) rainy events with media-high precipitation rates are more common in summer than in winter; (3) current satellite-based retrieval algorithms are limited in capturing short-lived convective storms or warm rain processes caused by climate and

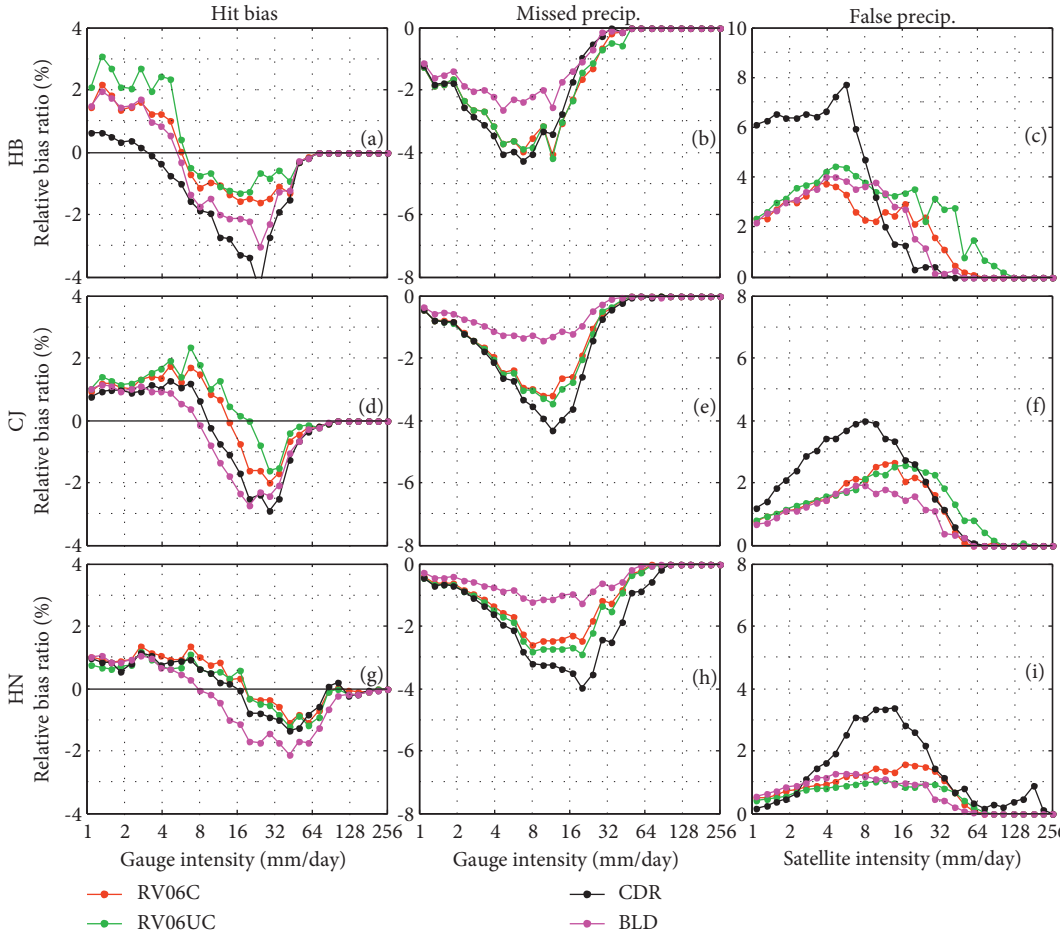

Figure 23: Same as Figure 20, but for winter seasons.

topography; and (4) precipitation retrieval algorithms are inclined to misrepresent the small and sparse rain events.

For FP, similar results to those of MP can be seen in summer. However, in winter, FP events are somewhat different than those of MP. For example, the largest relative bias ratio in FP for the RV06C and RV06UC products occurs over the semi-humid DB (Figure 22(i)) subregion; moreover, the relative bias ratio over the DB subregion is much larger than that over the arid XJ subregion (Figure 21(f)).

Appendix G lists the contribution ratios of the error components (hit, missed, and false) to the total bias of RV06C, RV06UC, CDR, and BLD.

In summertime, for the four satellite-based products, FP has the largest contribution to the total bias among hit bias, missed bias, and FP metrics for all regions (except for RV06UC over TP). During the transition from arid to wetter regions, FP rate shows a decreasing tendency. For the four SPPs, the largest contribution ratios for FP consistently occur over the arid XJ subregion and the smallest ones over the humid HN subregion. For example, the false bias for RV06UC reaches 99% over the arid XJ subregion, while the corresponding value of the humid region (HN) is 28.06%. Generally, the hit biases of the two IMERG products exhibit the smallest contribution to the total bias over most regions (except for HN). Meanwhile, except for CDR over TP, the hit biases of all four products are always negative. The gauge adjustments applied to RV06C have a relatively larger effect on hit bias and FP metrics than on MP since the MP rate for the two IMERG products is quite similar. That is to say, the gauge adjustment retrieval algorithms mainly improve the hit bias and FP to reduce total bias. At the same time, the total biases of the RV06C product are smaller than that of RV06UC in almost all regions in summer and winter (except for Mainland China, and the YG and HN subregions during the summer). RV06C changes RV06UC's underestimation with total biases of 11.53% vs. −24.47% over TP and 5.72% vs. −0.59% over YG in summer.

Moving from summer to winter in the same region, we find that the proportion of MP obviously increases substantially, especially for the two IMERG products. In fact, within the two IMERG products, the contribution ratios of MP to the total bias are the largest ones over most regions except for RV06C and RV06UC over the DB and HB subregions, and RV06UC over the CJ subregion. However, for the CDR and BLD products, the largest contribution ratio to total bias is still FP over almost all regions (except for CDR over the HN subregion). In wintertime, RV06UC total biases are negative over Mainland China and the XJ, TP, XB, YG, and HN subregions. RV06C improves upon RV06UC's underestimation over these regions, but the biases are still

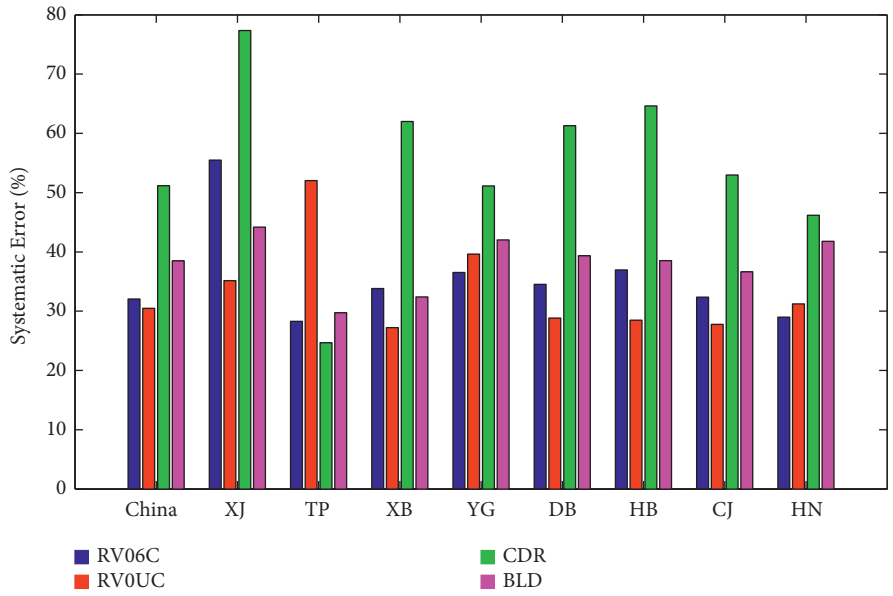

Figure 24: The proportion of systematic errors for the four satellite-based products' daily precipitation over Mainland China and the eight subregions during the period from March 2014 to June 2018.

negative. In wintertime, RV06C also relatively improves RV06UC's MP which is better than that in summer.

The sum of *Ran d* and *Syst* is 100%. Hence, only the proportion of systematic errors of the four satellite-based products' daily precipitation data is displayed in Figure 24. RV06, CDR, and BLD have larger systematic errors over XJ than Mainland China and other subregions. This result indicates that there is a large room for improvement in retrieval algorithms over the arid XJ subregion. The larger systematic errors over XJ have been noted previously by Tang [42]. Over Mainland China and most subregions (except for XJ region), the differences between systematic errors of RV06C, RV06UC, and BLD are not obvious. Among the four SPPs, CDR has the largest systematic errors over Mainland China and most subregions (except for XJ region), while RV06UC has the lowest systematic errors over Mainland China and most subregions (except for TP, YG, and HN subregions).

4. Discussion

In this study, an intercomparison between gauged-calibrated RV06C and uncalibrated RV06UC is conducted to investigate the impact of gauge adjustment. Meanwhile, a similar comparison is also performed between the IMERG, CDR, and BLD products to examine retrieval algorithm difference between satellite-based products. This comparison is intended to explore differences and similarities of the satellite-based products with different retrieval algorithms. Conventional precipitation assessments compare satellite-based precipitation estimates against gauge-based or ground-based radar precipitation observations directly with continuous statistical metrics or categorical statistics to obtain overall performance of satellite precipitation. However, these conventional approaches often fail to answer the question where the errors are from. To solve this problem, Tian et al. [33] introduced an error decomposition technique to separate total retrieval bias into three error components. Here, the conventional precipitation evaluation ways and the error decomposition analysis are utilized together to provide an in-depth exploration of the error features.

Within China, flood and drought are two mainly destructive natural disasters. According to Gebregiorgis et al. [37], different sources are responsible for different errors. For these reasons, the error features of satellite-based precipitation estimates are analyzed specifically in summer (rain season) and winter (dry season). In the future study, an evaluation including satellite-based satellite precipitation estimates' predictive ability of streamflow rate in a hydrological modeling framework should be conducted.

The four satellite-based precipitation estimates are systematically evaluated against 2088 separate automatic meteorological stations over China. However, a relatively sparse gauge network still occurs over some subregions (such as XJ and TP). Tian et al. [60] indicated that the dense rain-gauge network shows better assessment metrics of SPPs except for POD. That is to say, the sparse station distribution may increase uncertainty in our evaluations. Future work is needed to assess the satellite precipitation through more ground-based precipitation observations.

5. Summary and Conclusions

In this paper, the latest IMERG V06C and V06UC precipitation products are systematically evaluated over Mainland China and eight Chinese subregions during the period from March 2014 to June 2018 via statistical indices against the observation precipitation estimates from 2088 separate gauges. As a point of reference, CDR and BLD precipitation products are also investigated (in parallel with

the two IMERG precipitation products). In this process, the overall performance of the four SPPs is cross-compared and quantified at regional and national scales. For further analysis, the seasonal (summer and winter) error features of the error components are analyzed separately, and the contribution ratios of the error components to the total bias of satellite-based precipitation are investigated. Our main findings are as follows:

(1) In comparison with the precipitation observations of gauges, the four SPPs can generally capture the spatial distribution of precipitation over Mainland China. Meanwhile, according to relatively higher r values and lower RBs occurring over humid regions, the SPPs agree better with ground-based precipitation observations over humid regions than with those over semi-humid, semi-arid, and arid regions.

(2) According to the conventional evaluation way, among the four satellite-based products, CDR performs the worst with the lowest r values regardless of region and the highest RMSEs and MAEs over most subregions. As for the two latest IMERG products, RV06C has improved the performance of RV06UC with slightly larger r values in all subregions and smaller RMSEs and MAEs over Mainland China and most subregions (XJ, XB, DB, HB, and CJ). In the end, BLD shows the best performance with the highest r values and lowest MAEs and RMSEs over each region and the lowest RBs over most regions (China, TP, XB, DB, HB, CJ, and HN).

(3) Over the cold TP subregion, IMERG RV06UC severely underestimates area-average precipitation with a highly negative RB (−25.66%); however, CDR significantly overestimates it with a strongly positive RB (50.8%). Meanwhile, the calibrated RV06C prominently improves RV06UC's precipitation underestimation with better RB (11.5%), and BLD has the best performance with the smallest RB (10.04%).

(4) Except for the XJ subregion and RV06UC over the cold TP subregion, all four SPPs demonstrate relatively high POD (>0.5613). Likewise, all four SPPs have relatively low CSI (<0.5362) and high values of FAR (>0.3814) over all regions. At the same time, BLD has the highest values of POD over Mainland China and most of the examined subregions (except for XJ and TP) and provides the highest CSI over each region. RV06C shows slightly better scores of CSI and POD than RV06UC regardless of region (and for POD, except in the HB subregion), and CDR has the worst CSI and FAR scores over all regions. Across all subregions, all of the four SPPs have their worst performance (i.e., highest FARs and lowest PODs and CSIs) over the arid XJ region. All four precipitation products must improve their quality before they can be applied with confidence within the XJ subregion.

(5) The regional time series analyses clearly show that the total bias results from the interaction of the three independent error components (hit bias, MP, and FP). The error components of the four SPPs show strong regional and seasonal differences over Mainland China. The positive false error plays a remarkable role in the total bias of the four SPPs because the amplitude of FP is relatively larger than hit and missed precipitation, most of the time (Figures 9(a)–9(d)). For the two IMERG products, the calibrated RV06C improves upon the uncalibrated RV06UC's performance over most subregions, especially over TP and XJ; meanwhile, the result of adjustment for RV06C is better over dry regions (XJ and XB) and semi-humid regions (DB and HB) than over humid regions (YG, CJ, and HN). Generally speaking, among the four SPPs, CDR shows the worst performance with the highest amplitude of false error, hit bias, and total bias over Mainland China, while BLD has the best performance with the smallest amplitude of false error, missed error, and total bias (Figures 9(a)–9(d)).

(6) From the perspective of intensity distribution, for summer, over China, the four SPPs generally overestimate light precipitation and moderate precipitation events (<25 mm/day) and underestimate heavy precipitation events (>42 mm/day). Compared with RV06UC, the most remarkable improvement of RV06C occurs over TP, where calibrated RV06C provides an upward adjustment and therefore concentrates precipitation with precipitation rates from 4 mm/day to 64 mm/day against the uncalibrated RV06UC product. For the four SPPs, large FP rates play a dominant role in total bias in summer and winter. From summer to winter, the proportion of MP in total bias clearly increases. At the same time, the amplitude of CDR FP is usually the largest for light or moderate precipitation events, which contributes to CDR's overall poor performance.

(7) The relative bias ratio analysis shows that the contribution of MP seems to be lower over wetter regions. Moreover, for the same climate region, the contribution of MP is obviously lower in summer than in winter. For IMERG products, the gauge adjustments of RV06C have little effect on missed precipitation rates. However, the gauge adjustments have relatively bigger influence on missed rainy events in winter than in summer. In summer, for the four satellite-based products, the FP rate has the largest contribution to the total bias among hit bias, missed bias, and FP components over each region (except for RV06UC over the TP subregion). With a transition from arid region to the wetter and wetter regions, the FP rate shows a decreasing tendency. Generally speaking, the difference of error components for the four SPPs is relatively clearer in winter than in summer.

This analysis provides important insight regarding the spatiotemporal error characteristics of the IMERG V06C, IMERG V06UC, CDR, and BLD precipitation products over the eight subregions and all of Mainland China. Based on our research, large effort should be done to reduce missed snowing events in winter and FP of the four satellite-based products. An enhanced understanding of the structures and features of error components for the four SPPs is valuable for satellite precipitation data users to better apply data for applications in hydrologic forecasting, water resource management, and hydro-meteorological disaster prediction. Moreover, results are beneficial for future development of the satellite-based precipitation production algorithms.

Data Availability

The BLD precipitation datasets were downloaded from ftps://ftp.cpc.ncep.noaa.gov/precip/. CDR precipitation datasets were downloaded from ftps://persiann.eng.uci.edu/pub/. IMERG V06 precipitation product datasets during the study period from 12 March 2014 to 30 June 2018 were obtained from https://pmm.nasa.gov/data-access/downloads/gpm. The China Meteorological Administration (CMA) provided and calibrated the daily precipitation datasets of 2088 separate automatic meteorological stations.

Conflicts of Interest

The authors declare no conflicts of interest.

Authors' Contributions

Haishen Lu, Wade T. Crow, Yonghua Zhu, and Guanghua Wei contributed to conceptualization and methodology. Guanghua Wei participated in validation, prepared the original draft, and revised and edited the paper. Haishen Lu, Wade T. Crow, Jianbin Su, and Li Ren revised the paper.

Acknowledgments

This research was supported by the National Key Research and Development Program (Grant No. 2019YFC1510504); the NNSF (Grant Nos. 41830752, 42071033, and 41961134003); the National Natural Science Foundation of China (Grant No. 4210011922); and the Research Foundation of Jinling Institute of Technology (Grant No. jit-b-202206).

Supplementary Materials

The supplementary materials include Appendices A–G. Appendix A describes the characteristics of the eight subregions within Mainland China. Appendix B is the contingency table for comparing satellite precipitation and gauge observation. Appendix C gives the description of continuous and categorical statistical metrics used for the pairwise comparison between the SPPs and gauged observations. Appendix D describes the error decomposition and relative bias ratio (RBR). Appendix E shows the area-averaged values of r, RB, RMSE, and MAE for the four satellite-based products over Mainland China and the eight subregions from March 2014 to June 2018. Appendix F shows relative bias ratio (RBR) for the hit bias (HB), negative hit bias (NHB), and positive hit bias (PHB). Appendix G describes the area-averaged contribution ratio (%) of the error components to total bias of RV06C, RV06UC, CDR, and BLD for winter and summer seasons over Mainland China and the eight selected subregions. (*Supplementary Materials*)

References

[1] S. Ma and T. Zhou, "Observed trends in the timing of wet and dry season in China and the associated changes in frequency and duration of daily precipitation," *International Journal of Climatology*, vol. 35, no. 15, pp. 4631–4641, 2015.

[2] C. Lai, R. Zhong, Z. Wang et al., "Monitoring hydrological drought using long-term satellite-based precipitation data," *The Science of the Total Environment*, vol. 649, pp. 1198–1208, 2019.

[3] P. Zhai, X. Zhang, H. Wan, and X. Pan, "Trends in total precipitation and frequency of daily precipitation extremes over China," *Journal of Climate*, vol. 18, no. 7, pp. 1096–1108, 2005.

[4] A. Y. Hou, R. K. Kakar, S. Neeck et al., "The global precipitation measurement mission," *Bulletin of the American Meteorological Society*, vol. 95, no. 5, pp. 701–722, 2014.

[5] F. Lo Conti, K. L. Hsu, L. V. Noto, and S. Sorooshian, "Evaluation and comparison of satellite precipitation estimates with reference to a local area in the Mediterranean Sea," *Atmospheric Research*, vol. 138, pp. 189–204, 2014.

[6] A. T. Haile, F. Yan, and E. Habib, "Accuracy of the cmorph satellite-rainfall product over lake Tana basin in eastern Africa," *Atmospheric Research*, vol. 163, pp. 177–187, 2015.

[7] G. H. Wei, H. S. Lü, W. T Crow, Y. H. Zhu, J. Q. Wang, and J. B. Su, "Evaluation of satellite-based precipitation products from imerg v04a and v03d, cmorph and tmpa with gauged rainfall in three climatologic zones in China," *Remote Sensing*, vol. 10, no. 2, p. 30, 2017.

[8] G. H. Wei, H. S. Lü, W. T. Crow, Y. H. Zhu, J. Q. Wang, and J. B. Su, "Comprehensive evaluation of gpm-imerg, cmorph, and tmpa precipitation products with gauged rainfall over mainland China," *Advances in Meteorology*, vol. 2018, Article ID 3024190, 18 pages, 2018.

[9] J. Su, H. Lü, Y. Zhu, X. Wang, and G. Wei, "Component analysis of errors in four gpm-based precipitation estimations over mainland China," *Remote Sensing*, vol. 10, no. 9, p. 1420, 2018.

[10] B. Yong, B. Chen, Y. Tian, Z. Yu, and Y. Hong, "Error-component analysis of trmm-based multi-satellite precipitation estimates over mainland China," *Remote Sensing*, vol. 8, no. 5, p. 440, 2016.

[11] D. F. Barrera, E. Ceirano, and G. V. Zucarelli, "Differences in area-averaged rainfall depth over a mid-size basin from two remote sensing methods of estimating precipitation," in *Predictions in Ungauged Basins: Pub Kick-Off*IAHS Publication, London, UK, 2007.

[12] H. Guo, S. Chen, A. Bao, J. Hu, B. Yang, and P. Stepanian, "Comprehensive evaluation of high-resolution satellite-based precipitation products over China," *Atmosphere*, vol. 7, no. 1, p. 6, 2015.

[13] H. Guo, S. Chen, A. Bao et al., "Early assessment of integrated multi-satellite retrievals for global precipitation measurement

over China," *Atmospheric Research*, vol. 176-177, pp. 121–133, 2016.

[14] G. Tang, Y. Ma, D. Long, L. Zhong, and Y. Hong, "Evaluation of gpm day-1 imerg and tmpa version-7 legacy products over mainland China at multiple spatiotemporal scales," *Journal of Hydrology*, vol. 533, pp. 152–167, 2016.

[15] F. Chen and X. Li, "Evaluation of imerg and trmm 3b43 monthly precipitation products over mainland China," *Remote Sensing*, vol. 8, no. 6, p. 472, 2016.

[16] S. Chen, Y. Hong, J. J. Gourley et al., "Evaluation of the successive v6 and v7 trmm multisatellite precipitation analysis over the continental United States," *Water Resources Research*, vol. 49, no. 12, pp. 8174–8186, 2013.

[17] G. J. Huffman, D. T. Bolvin, E. J. Nelkin et al., "The trmm multisatellite precipitation analysis (tmpa): quasi-global, multiyear, combined-sensor precipitation estimates at fine scales," *Journal of Hydrometeorology*, vol. 8, no. 1, pp. 38–55, 2007.

[18] S. Sorooshian, K. L. Hsu, X. Gao, H. V. Gupta, B. Imam, and D. Braithwaite, "Evaluation of persiann system satellite–based estimates of tropical rainfall," *Bulletin of the American Meteorological Society*, vol. 81, no. 9, pp. 2035–2046, 2000.

[19] R. J. Joyce, J. E. Janowiak, P. A. Arkin, and P. Xie, "Cmorph: a method that produces global precipitation estimates from passive microwave and infrared data at high spatial and temporal resolution," *Journal of Hydrometeorology*, vol. 5, pp. 287–296, 2004.

[20] G. J. Huffman, D. T. Bolvin, D. Braithwaite et al., *Algorithm Theoretical Basis Document (atbd) Version 4.5: Nasa Global Precipitation Measurement (gpm) Integrated Multi-Satellite Retrievals for gpm (imerg)*, NASA/GSFC, Greenbelt, MD, USA, 2015.

[21] G. J. Huffman, D. T. Bolvin, D. Braithwaite et al., *Algorithm Theoretical Basis Document (atbd) Version 06: Nasa Global Precipitation Measurement (gpm) Integrated Multi-Satellite Retrievals for gpm (imerg)*, NASA/GSFC, Greenbelt, MD, USA, 2019.

[22] G. J. Huffman, D. T. Bolvin, E. J. Nelkin, E. F. Stocker, and J. Tan, *V06 Imerg Final Run Release Notes*, NASA/GSFC, Greenbelt, MD, USA, 2019.

[23] B. Yong, Y. Hong, L. L. Ren et al., "Assessment of evolving trmm-based multisatellite real-time precipitation estimation methods and their impacts on hydrologic prediction in a high latitude basin," *Journal of Geophysical Research: Atmospheres*, vol. 117, no. D9, p. 9108, 2012.

[24] H. Zhao, S. Yang, S. You, Y. Huang, Q. Wang, and Q. Zhou, "Comprehensive evaluation of two successive v3 and v4 imerg final run precipitation products over mainland China," *Remote Sensing*, vol. 10, no. 2, p. 34, 2017.

[25] H. Zhao, B. Yang, S. Yang et al., "Systematical estimation of gpm-based global satellite mapping of precipitation products over China," *Atmospheric Research*, vol. 201, pp. 206–217, 2018.

[26] Y. Shen, P. Zhao, Y. Pan, and J. Yu, "A high spatiotemporal gauge-satellite merged precipitation analysis over China," *Journal of Geophysical Research Atmospheres*, vol. 119, no. 6, pp. 3063–3075, 2014.

[27] W. Wang, H. Lu, T. Zhao, L. Jiang, and J. Shi, "Evaluation and comparison of daily rainfall from latest gpm and trmm products over the Mekong river basin," *IEEE Journal of Selected Topics in Applied Earth Observations and Remote Sensing*, vol. 10, no. 6, pp. 2540–2549, 2017.

[28] F. Porcù, L. Milani, and M. Petracca, "On the uncertainties in validating satellite instantaneous rainfall estimates with raingauge operational network," *Atmospheric Research*, vol. 144, pp. 73–81, 2014.

[29] M. Petracca, L. P. D'Adderio, F. Porcù, G. Vulpiani, and S. Sebastianelli, "Validation of gpm dual-frequency precipitation radar (dpr) rainfall products over Italy," *Journal of Hydrometeorology*, vol. 19, no. 5, pp. 907–925, 2018.

[30] Y. Shen, A. Xiong, Y. Wang, and P. Xie, "Performance of high-resolution satellite precipitation products over China," *Journal of Geophysical Research*, vol. 115, no. D2, p. 2114, 2010.

[31] P. Salio, M. P. Hobouchian, Y. García Skabar, and D. Vila, "Evaluation of high-resolution satellite precipitation estimates over southern south America using a dense rain gauge network," *Atmospheric Research*, vol. 163, pp. 146–161, 2015.

[32] V. Maggioni, P. C. Meyers, and M. D. Robinson, "A review of merged high-resolution satellite precipitation product accuracy during the tropical rainfall measuring mission (trmm) era," *Journal of Hydrometeorology*, vol. 17, no. 4, pp. 1101–1117, 2016.

[33] Y. Tian, C. D. Peters-Lidard, J. B. Eylander et al., "Component analysis of errors in satellite-based precipitation estimates," *Journal of Geophysical Research*, vol. 114, no. D24, p. 101, 2009.

[34] L. Tang, Y. Tian, F. Yan, and E. Habib, "An improved procedure for the validation of satellite-based precipitation estimates," *Atmospheric Research*, vol. 163, pp. 61–73, 2015.

[35] S. Xu, Y. Shen, and Z. Du, "Tracing the source of the errors in hourly imerg using a decomposition evaluation scheme," *Atmosphere*, vol. 7, no. 12, p. 161, 2016.

[36] S. Ning, F. Song, P. Udmale, J. Jin, B. R. Thapa, and H. Ishidaira, "Error analysis and evaluation of the latest gsmap and imerg precipitation products over eastern China," *Advances in Meteorology*, vol. 2017, Article ID 1803492, 16 pages, 2017.

[37] A. S. Gebregiorgis, Y. Tian, C. D. Peters-Lidard, and F. Hossain, "Tracing hydrologic model simulation error as a function of satellite rainfall estimation bias components and land use and land cover conditions," *Water Resources Research*, vol. 48, no. 11, p. 11509, 2012.

[38] M. N. Anjum, I. Ahmad, Y. Ding et al., "Assessment of imerg-v06 precipitation product over different hydro-climatic regimes in the Tianshan mountains, north-western China," *Remote Sensing*, vol. 11, no. 19, pp. 2314–2336, 2019.

[39] S. Jiang, L. Wei, L. Ren et al., "Utility of integrated imerg precipitation and gleam potential evapotranspiration products for drought monitoring over mainland China," *Atmospheric Research*, vol. 247, Article ID 105141, 2021.

[40] L. Y. Wei, S. H. Jiang, L. L. Ren, L. Q. Zhang, M. H. Wang, and Z. Duan, "Preliminary utility of the retrospective imerg precipitation product for large-scale drought monitoring over mainland China," *Remote Sensing*, vol. 12, no. 18, p. 2993, 2020.

[41] Q. Ma, Y. Li, H. Feng et al., "Performance evaluation and correction of precipitation data using the 20-year imerg and tmpa precipitation products in diverse subregions of China," *Atmospheric Research*, vol. 249, 2020.

[42] G. Tang, M. P. Clark, S. M. Papalexiou, Z. Ma, and Y. Hong, "Have satellite precipitation products improved over last two decades? A comprehensive comparison of gpm imerg with nine satellite and reanalysis datasets," *Remote Sensing of Environment*, vol. 240, Article ID 111697, 2020.

[43] Z. Zhou, B. Guo, W. Xing, J. Zhou, and F. Xu, "Comprehensive evaluation of latest gpm era imerg and gsmap

precipitation products over mainland China," *Atmospheric Research*, vol. 246, Article ID 105132, 2020.

[44] X. Li, O. Sungmin, N. Wang, L. Liu, and Y. Huang, "Evaluation of the gpm imerg v06 products for light rain over mainland China," *Atmospheric Research*, vol. 253, Article ID 105510, 2021.

[45] L. Y. Wei, S. H. Jiang, L. L. Ren et al., "Evaluation of seventeen satellite-, reanalysis-, and gauge-based precipitation products for drought monitoring across mainland China—sciencedirect," *Atmospheric Research*, vol. 263, 2021.

[46] Y. Zhang, A. Ye, P. Nguyen, B. Analui, and S. Sorooshian, "New insights into error decomposition for precipitation products," *Geophysical Research Letters*, vol. 48, no. 17, 2021.

[47] P. Xie, M. Chen, S. Yang et al., "A gauge-based analysis of daily precipitation over east Asia," *Journal of Hydrometeorology*, vol. 8, no. 3, pp. 607–626, 2007.

[48] Y. Shen and A. Xiong, "Validation and comparison of a new gauge-based precipitation analysis over mainland China," *International Journal of Climatology*, vol. 36, no. 1, pp. 252–265, 2016.

[49] S. Chen, Y. Hong, Q. Cao et al., "Similarity and difference of the two successive v6 and v7 trmm multisatellite precipitation analysis performance over China," *Journal of Geophysical Research Atmospheres*, vol. 118, no. 23, pp. 13060–13074, 2013.

[50] R. Yu, T. Zhou, A. Xiong, Y. Zhu, and J. Li, "Diurnal variations of summer precipitation over contiguous China," *Geophysical Research Letters*, vol. 34, no. 1, pp. 223–234, 2007.

[51] R. J. Joyce, P. Xie, Y. Yarosh, J. E. Janowiak, and P. A. Arkin, "Cmorph: a "morphing" approach for high resolution precipitation product generation," in *Satellite Rainfall Applications for Surface Hydrology*, pp. 23–37, Springer, Berlin, Germany, 2010.

[52] E. Habib, A. T. Haile, Y. Tian, and R. J. Joyce, "Evaluation of the high-resolution cmorph satellite rainfall product using dense rain gauge observations and radar-based estimates," *Journal of Hydrometeorology*, vol. 13, no. 6, pp. 1784–1798, 2012.

[53] M. Faridzad, T. T. Yang, K. Hsu, S. Sorooshian, and C. Xiao, "Rainfall frequency analysis for ungauged regions using remotely sensed precipitation information," *Journal of Hydrology*, vol. 563, pp. 123–142, 2018.

[54] H. Ashouri, K. L. Hsu, S. Sorooshian et al., "Persiann-cdr: daily precipitation climate data record from multisatellite observations for hydrological and climate studies," *Bulletin of the American Meteorological Society*, vol. 96, no. 1, pp. 69–83, 2015.

[55] B. Yong, L. L. Ren, Y. Hong et al., "Hydrologic evaluation of multisatellite precipitation analysis standard precipitation products in basins beyond its inclined latitude band: a case study in Laohahe basin, China," *Water Resources Research*, vol. 46, no. 7, pp. 759–768, 2010.

[56] B. Ahrens, "Distance in spatial interpolation of daily rain gauge data," *Hydrology and Earth System Sciences*, vol. 10, no. 2, pp. 197–208, 2006.

[57] K. Tong, F. Su, D. Yang, L. Zhang, and Z. Hao, "Tibetan plateau precipitation as depicted by gauge observations, reanalyses and satellite retrievals," *International Journal of Climatology*, vol. 34, no. 2, pp. 265–285, 2014.

[58] X. H. Tan, B. Yong, and L. L. Ren, "Error features of the hourly gsmap multi-satellite precipitation estimates over nine major basins of China," *Hydrology Research*, vol. 49, no. 3, pp. 761–779, 2018.

[59] S. Palomino-Angel, J. A. Anaya-Acevedo, and B. A. Botero, "Evaluation of 3b42v7 and imerg daily-precipitation products for a very high-precipitation region in northwestern south America," *Atmospheric Research*, vol. 217, pp. 37–48, 2019.

[60] F. Tian, S. Hou, L. Yang, H. Hu, and A. Hou, "How does the evaluation of gpm imerg rainfall product depend on gauge density and rainfall intensity?" *Journal of Hydrometeorology*, vol. 19, 2017.